

# GEASI: Geodesic-based Earliest Activation Sites Identification in cardiac models

Thomas Grandits<sup>1,4</sup>, Alexander Effland<sup>1,5</sup>, Thomas Pock<sup>1,4</sup>, Rolf Krause<sup>2</sup>, Gernot Plank<sup>3,4</sup>, and Simone Pezzuto<sup>2</sup>

<sup>1</sup>*Institute of Computer Graphics and Vision, TU Graz, Inffeldgasse 16, 8010 Graz, Austria*

<sup>2</sup>*Center for Computational Medicine in Cardiology, Institute of Computational Science, Università della Svizzera italiana, via G. Buffi 13, 6900 Lugano, Switzerland*

<sup>3</sup>*Gottfried Schatz Research Center - Division of Biophysics, Medical University of Graz, Neue Stiftingtalstraße 6/IV, 8010 Graz, Austria*

<sup>4</sup>*BioTechMed-Graz, Graz, Austria*

<sup>5</sup>*Silicon Austria Labs (TU Graz SAL DES Lab), Graz, Austria*

## Abstract

The personalization of cardiac models is the cornerstone of patient-specific modeling. Ideally, non-invasive or minimally-invasive clinical data, such as the standard ECG or intracardiac contact recordings, could provide an insight on model parameters. Parameter selection of such models is however a challenging and potentially time-consuming task.

In this work, we estimate the earliest activation sites governing the cardiac electrical activation. Specifically, we introduce GEASI (**G**eodesic-based **E**arliest **A**ctivation **S**ites **I**dentification) as a novel approach to simultaneously identify their locations and times. To this end, we start from the anisotropic eikonal equation modeling cardiac electrical activation and exploit its Hamilton–Jacobi formulation to minimize a given objective functional, which in the case of GEASI is the quadratic mismatch to given activation measurements. This versatile approach can be extended for computing topological gradients to estimate the number of sites, or fitting a given ECG.

We conducted various experiments in 2D and 3D for in-silico models and an in-vivo intracardiac recording collected from a patient undergoing cardiac resynchronization therapy. The results demonstrate the clinical applicability of GEASI for potential future personalized models and clinical intervention.

## 1 Introduction

In this work, we address the central question of identifying earliest activation sites (EASs). In a healthy (human) heart, the spontaneous electric activity of the sino-atrial node initiates an electric wave that first spreads across the atria, and then propagates through the ventricles via the atrio-ventricular node/His bundle/Purkinje network pathway. In patient-specific models, the EASs determine many physiological phenomena such as the Purkinje entry points. For these phenomena, a proper manual quantification is in practice infeasible, especially in the presence of pathological conditions such as bundle branch block, ventricular tachycardia or premature ventricular contractions. Thus, inter-patient variability of electrical activation necessitates automatic individual parameter identification. The identification of earliest activation sites, possibly from non-invasive or minimally-invasive recordings, is therefore of clinical relevance for a correct diagnosis and optimal treatment.

Indeed, a grand challenge in cardiac modeling for personalized health care is the aforementioned individualization of the model parameters for given patient data, which may include standard imaging, electrocardiogram (ECG), or invasive mapping. A particularly suitable model that exposes EASs is the eikonal equation, which was originally exploited as a convenient approximation of the monodomain and bidomain models [26, 11] and is nowadays more often utilized for its computational efficiency [30]. In this work, we present a novel gradient-based approach for localizing the

EASs termed GEASI (**G**eodesic-based **E**arliest **A**ctivation **S**ites **I**dentification). We start from the anisotropic eikonal equation as a common model for cardiac electrophysiology [10], in which the EASs define boundary conditions at specific sites. The anisotropy arises from the fiber alignment inside the heart [11]. For numerical reasons, the eikonal equation is solved using the Fast Iterative Method (FIM) [20]. The main goal of our approach is the minimization of a given objective functional depending on the solution of the anisotropic eikonal equation as a function of the EASs. Here, a feasible optimization strategy involves the Hamilton–Jacobi formalism, which promotes a tractable derivative with respect to the EASs [15]. Note that this derivative is geometrically related to the tangent of the geodesic at the EASs. In this respect, a geodesic connects an EAS such as a Purkinje entry point to an observation through a path of minimum distance in a predefined metric. Finally, we exploit the aforementioned methods to introduce GEASI, which in its core employs a quadratic mismatch between the eikonal solution and the measurements in the objective functional.

We emphasize that our method is not limited to this quadratic objective functional and can straightforwardly be extended to other scenarios. In this work, we additionally investigate two such extensions: the topological gradient and the fitting of an eikonal solution to a target ECG.

The topological gradient allows for an estimation of the optimal number of EASs. In detail, the concept of topological gradient can be readily introduced via the Hamilton–Jacobi theory. Here, we consider a splitting of a single EAS into a pair of two EASs symmetrically arranged at infinitesimal distance along a given direction in a dipole-like fashion. Thus, the topological gradient provides a criterion to decide if an EAS should be split. In particular, this approach promotes a simple model as a starting point with too little complexity to represent the measurement data and increase the number of source sites until the encountered activations are properly approximated.

In combination with the bidomain equation and the lead field theory, the eikonal model also results in an almost-real-time ECG simulator [33] with remarkable physiological accuracy [10]. Efficient combinations with other methods exist to use solutions of the eikonal equation to compute surface ECGs and body surface potential mappings (BSPMs) [33], [30], making these methods a very powerful computational tool. We here employ the existing approach [33] to solve the inverse ECG problem, i.e. we introduce a method to localize EASs purely from ECG data. Numerical experiments in Section 5 demonstrate that the proposed approach is capable of finding the optimal EASs even in high-fidelity cardiac models.

## 1.1 Related Work

In what follows, we briefly review similar and related approaches to GEASI.

From a physiological perspective, EASs can be considered as end-points or junctions of the Purkinje network [14]. This method closely follows the actual anatomy of the heart [41], and it is indicated in the case of a healthy activation and a (complete or partial) bundle branch block. When dense endocardial mapping data are available, the Purkinje network can be estimated automatically [32, 2, 40]. However, reconstructing the network from remote (e.g. the ECG or epicardial mapping) or sparse endocardial recordings is challenging.

An alternative formulation is based on a very sparse set of EASs embedded in thin, fast-conducting layers in both ventricular endocardia [29]. In some sense, this approach can be referred to as *lumped Purkinje network* formulation. Here, the number of EASs is drastically reduced. In fact, a few sites per chamber are generally sufficient to correctly capture the activation and reproduce the surface ECG [35].

Overall, the parameters of the eikonal model with lumped Purkinje network are just the location, the number and the activation onset of the EASs, as well as the conduction velocities in the thin layers and the myocardium. The problem of fitting these parameters to clinical data has already been considered in the literature for the conduction velocities [3, 24, 38, 23]. However, the optimization of EASs received limited attention so far with only a few works dealing with activation onsets [25] or locations [27]. The simultaneous optimization of EASs (especially their number) and conduction velocity has been analyzed only very recently in [21, 23, 34].

In [32], Purkinje networks are created from intra-cardiac measurements by dividing the endocardium into regions of influence for each Purkinje entry point. For this purpose, an isotropic eikonal equation is solved for each measurement point to compute the regions of influence in a

Voronoi-diagram like fashion. According to fractal laws, Purkinje entry points are subsequently either moved, deleted or generated to better fit the observed activation on the endocardium. The connection with the presented approach becomes apparent once we consider the underlying problem in terms of geodesics and regions of influence, further discussed in Section 2. By definition, geodesics are locally unique length-minimizing paths and therefore yield an analogous partition of the domain. We can observe that our method is a generalization of the aforementioned approach in [32], since it gives rise to Voronoi partitions with non-linear boundaries. Thus, GEASI can therefore be applied to heterogeneous conduction velocities and heterogeneous fiber directions.

In the work by Kunisch et al. [27], the authors recast the problem of localizing EASs as a shape optimization problem. In their viscous eikonal formulation, the EASs are modelled as small spherical holes in the domain whose boundaries impose the activation onset. Under sufficient smoothness assumptions, an adjoint state can be defined through the shape derivative with respect to these boundaries, and therefore be exploited to optimize the EASs. This approach is efficient and can be applied to multiple pacing sites, although—in contrast to our approach—no topological changes are permitted by the formulation, impeding both a change in the number of EASs and movement from the interior to the boundary of the domain. Additionally, the coalescence of multiple sites needs special treatment in the shape derivative (not addressed in [27]). The viscous eikonal formulation, moreover, introduces a curvature-dependent conduction velocity, potentially strong at EASs, posing limitations on the radius of the spherical holes. It is worth noting that previous works including [27, 25] require local measurements of activation times, e.g. endocardial maps, whereas GEASI can be applied to fit epicardial recordings and even the surface ECG. This aspect is relevant in view of non-invasive personalization of patient-specific models, which was recently advocated in [13].

A major challenge in cardiac personalization is the estimation of the ground truth number of EASs. A possible solution is to consider a large number of EASs densely covering the earliest activation region, and successively removing sites according to some predefined rule [34]. For instance, an optimization procedure could determine the optimal activation onset of all sites, and then remove those with a very late onset. In a previous study, we optimized the initiation times along with the anisotropic conductivity tensors by differentiating the existing Fast Iterative Method solver introduced in [20]. The large number of EASs results in a highly ill-posed inverse problem and consequently requires further regularization to successively remove initiation sites. While providing good results with respect to the measured activation times [23, 34], this approach heavily relies on initial choice of EASs and the selected regularization strategy.

## 1.2 Notation

We denote the identity matrix by  $\mathbf{I}$  and the space of symmetric and positive definite matrices in  $\mathbb{R}^d$  by  $\text{Sym}^{d \times d}$ . Throughout this work,  $B_\zeta(\mathbf{x})$  and  $\overline{B}_\zeta(\mathbf{x})$  refer to the open and closed ball with radius  $\zeta > 0$  around  $\mathbf{x}$ .  $[A]_{ij}$  denotes the entry in the  $i$ -th row and  $j$ -th column of a matrix  $A \in \mathbb{R}^{n_1 \times n_2}$ . Furthermore,  $A \succ B$  if  $A - B$  is positive definite for  $A, B \in \text{Sym}^{d \times d}$ , and we set  $\llbracket N \rrbracket := \{1, \dots, N\}$ . The set of unit vectors in  $\mathbb{R}^d$  is denoted by  $\mathbb{S}^{d-1}$ . The Dirac measure of a set  $S$  is referred to as  $\delta_{[S]}$ . Further, we use the notation  $C^0(X, Y)$  for the space of continuous functions mapping from  $X$  to  $Y$  endowed with the norm  $\|\cdot\|_{C^0(X, Y)}$ , and we denote by  $C^k(X, Y)$  the associated space of  $k$ -times continuously differentiable functions equipped with the norm  $\|\cdot\|_{C^k(X, Y)}$ . We use the symbol  $C^{k, \alpha}(X, Y)$  for the Hölder space with exponent  $\alpha$  and norm  $\|\cdot\|_{C^{k, \alpha}(X, Y)}$ . Finally, we denote by  $L^p(X, Y)$  and  $W^{m, p}(X, Y)$  the  $p$ -Lebesgue space and the Sobolev space of  $m$ -times weakly differentiable and  $p$ -integrable functions, and we set  $H^m(X, Y) = W^{m, 2}(X, Y)$ .

## 1.3 Structure of the Work

In Section 2, we successively introduce the eikonal equation and the objective functional, which are the building blocks of GEASI. Based on the introduced algorithm, we present in Section 3 the topological gradient as well as the ECG fitting problem. Then, we elaborate in Section 4 on efficient discretization schemes and implementation detail of the proposed method. In Section 5, we consider the problem of estimating the initiation sites for different models—primarily in-silico

experiments, but also one in-vivo experiment. Further aspects of future work are addressed in Section 6.

## 2 GEASI

Next, we introduce the GEASI method, which encompasses the following ingredients. In Section 2.1, we review the anisotropic eikonal equation and its associated Hamilton–Jacobi formulation. Subsequently, in Section 2.2 we analyze a general objective function involving the solution of the anisotropic eikonal equation from a functional-analytical perspective. Section 2.3 deals with the gradient computation of the distance function, which is later exploited in the aforementioned objective functional. Finally, all introduced concepts are combined in Section 2.4 to define GEASI.

### 2.1 Eikonal equation

We consider the computational domain  $\Omega \subset \mathbb{R}^d$  for  $d \geq 2$ , which in most cases represents the myocardium. Further, let  $\mathcal{E}$  be the subset of  $N$  pairs  $\{(\mathbf{x}_i, t_i)_{i=1}^N\} \in \mathcal{U}_N := \Omega^N \times (T_{\min}, T_{\max})^N$  for a priori given  $T_{\min} < T_{\max}$  and fixed  $N$ . Throughout this work,  $\mathcal{E}$  is a set of EASs, where  $N$  is the number of EASs,  $\mathbf{x}_i$  and  $t_i$  are the location and timing of the  $i$ -th site, respectively. Let  $\phi_{\mathcal{E}} : \Omega \rightarrow \mathbb{R}$  be the unique solution of the anisotropic eikonal equation with prescribed values on  $\mathcal{E}$ , which is commonly referred to as the activation map. Hence,  $\phi_{\mathcal{E}}$  solves

$$\begin{cases} \sqrt{\mathbf{D}(\mathbf{x}) \nabla \phi_{\mathcal{E}}(\mathbf{x}) \cdot \nabla \phi_{\mathcal{E}}(\mathbf{x})} = 1, & \mathbf{x} \in \Omega \setminus \{\mathbf{x}_1, \dots, \mathbf{x}_N\}, \\ \phi_{\mathcal{E}}(\mathbf{x}_i) = t_i, & (\mathbf{x}_i, t_i) \in \mathcal{E}, \end{cases} \quad (1)$$

where  $\mathbf{D} \in C^1(\bar{\Omega}, \text{Sym}^{d \times d})$  describes the anisotropic conduction. Recall that  $\text{Sym}^{d \times d}$  is defined as the set of positive definite and symmetric  $d \times d$ -matrices, which gives rise to the definition of the norm  $\|\mathbf{p}\|_{\mathbf{D}} := \sqrt{\mathbf{D}\mathbf{p} \cdot \mathbf{p}}$  for  $\mathbf{p} \in \mathbb{R}^d$ . Note that the assumptions already guarantee that

$$\lambda_* \mathbf{I} \prec \mathbf{D}(\mathbf{x}) \prec \lambda^* \mathbf{I}$$

for all  $\mathbf{x} \in \bar{\Omega}$  and finite bounds  $0 < \lambda_* \leq \lambda^* < \infty$ . It is well known that the eikonal equation (1) admits a unique viscosity solution according to the theory of Hamilton–Jacobi equations [15]. The Lipschitz continuous solution of the eikonal equation  $\phi_{\mathcal{E}} \in C^{0,1}(\bar{\Omega})$  is of the form

$$\phi_{\mathcal{E}}(\mathbf{x}) = \min_{(\mathbf{y}, t) \in \mathcal{E}} \{t + \delta(\mathbf{x}, \mathbf{y})\} \quad (2)$$

where  $\delta(\mathbf{x}, \mathbf{y})$  denotes the *geodesic distance*

$$\delta(\mathbf{x}, \mathbf{y}) = \inf_{\hat{\gamma} \in H^1([0,1], \bar{\Omega})} \{L(\hat{\gamma}) : \hat{\gamma}(0) = \mathbf{x}, \hat{\gamma}(1) = \mathbf{y}\} \quad (3)$$

given the length functional

$$L(\gamma) := \int_0^1 \|\dot{\gamma}(t)\|_{\mathbf{D}^{-1}(\gamma(t))} dt. \quad (4)$$

Thus, the induced Riemannian metric for two tangent vectors  $\mathbf{v}, \mathbf{w}$  is

$$\langle \mathbf{v}, \mathbf{w} \rangle_{\gamma(t)} := \mathbf{D}^{-1}(\gamma(t)) \mathbf{v} \cdot \mathbf{w}. \quad (5)$$

We note that the infimum  $\gamma$  in (3) is actually attained, and by the geodesic equation we can even deduce  $\gamma \in C^{0,1}([0,1], \bar{\Omega})$  (see e.g. [5]). Indeed, in the definition (3), we first note that  $\|\mathbf{p}\|_{\mathbf{D}^{-1}(\mathbf{x})} \leq \lambda_*^{-1} \|\mathbf{p}\|_2$  for all  $\mathbf{p} \in \mathbb{R}^d$  and  $\mathbf{x} \in \Omega$ . Then, for any segment  $[\mathbf{x}, \mathbf{y}]$  fully contained in  $\bar{\Omega}$  we have that  $\delta(\mathbf{x}, \mathbf{y}) \leq \lambda_*^{-1} \|\mathbf{x} - \mathbf{y}\|_2$  since the segment is a geodesic path in the Euclidean norm. Figure 1 illustrates a single geodesic path in red on a domain with a continuously varying conduction velocity and isotropic conduction.

When  $N > 1$ , all pairs  $(\mathbf{x}_i, t_i), (\mathbf{x}_j, t_j) \in \mathcal{E}$  must satisfy the subsequent compatibility condition

$$|t_i - t_j| \leq \delta(\mathbf{x}_i, \mathbf{x}_j) \quad (6)$$



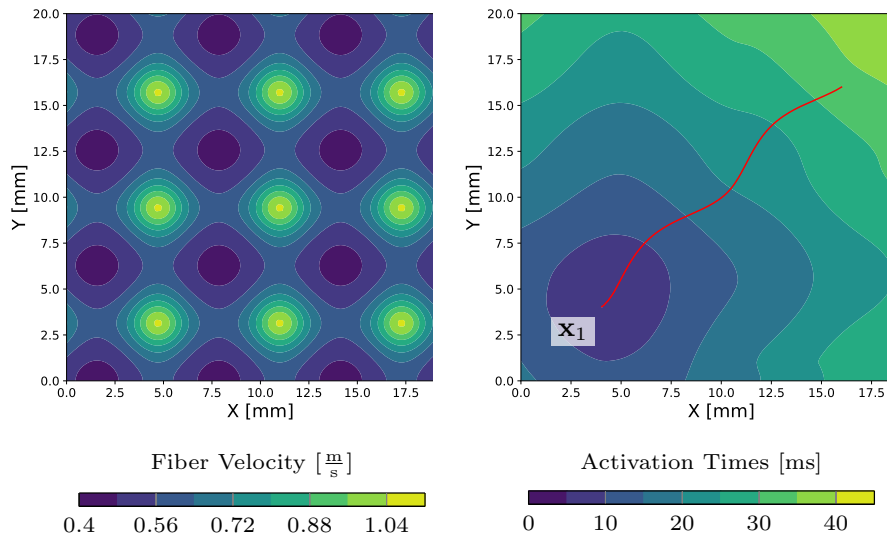


Figure 1: Left: fixed velocity field  $c$  in  $\Omega$ . Right: contour plot of the associated anisotropic eikonal equation with anisotropic conduction  $\mathbf{D}(\mathbf{x}) = c(\mathbf{x})^2 \mathbf{I}$  along with the geodesic path joining the EAS  $\mathbf{x}_1$  with an arbitrary point.

in order to ensure the existence of a solution. It is worth noting that this condition is not too restrictive. In view of (2), which underpins our numerical solution of the eikonal equation, non-compatible data are simply discarded. Interestingly, this is also physiologically sound: a stimulus applied in the depolarized region cannot trigger another propagation.

The Hamilton–Jacobi formulation is essential for computing perturbations of  $\mathcal{E}$ , which is conducted in the following subsection.

## 2.2 Objective functional

The overall objective of this work is the minimization of a given functional  $\mathcal{J} : C^{0,1}(\overline{\Omega}) \rightarrow \mathbb{R}$  depending on the activation map  $\phi_{\mathcal{E}}$  with respect to  $\mathcal{E}$ , i.e.

$$m_N := \min_{\mathcal{E} \in \mathcal{U}_N} \mathcal{J}(\phi_{\mathcal{E}}). \quad (7)$$

For instance, the objective could describe the minimization of a mismatch (in the least-squares sense) between the simulated activation and the activation detected from epicardial, as well as endocardial mapping (see Section 5). The objective functional can also involve the activation map implicitly: In Section 5.3, we utilize the mismatch between the recorded and simulated 12-lead surface ECG as a metric for optimization.

In what follows, we prove the existence of minimizers for (7) for varying  $N$ . To this end, we define for  $\mathcal{E} = \{(\mathbf{x}_i, t_i)_{i=1}^N\}$

$$\Phi_N(\mathbf{x}, \mathbf{x}_1, \dots, \mathbf{x}_N, t_1, \dots, t_N) := \phi_{\mathcal{E}}(\mathbf{x}). \quad (8)$$

**Lemma 1.**  $\Phi_N \in C^{0,1}(\overline{\Omega \times \mathcal{U}_N})$  is a bounded function of its arguments.

*Proof.* Using (2), we immediately see that

$$\Phi_N(\mathbf{x}, \mathbf{x}_1, \dots, \mathbf{x}_N, t_1, \dots, t_N) = \min_{i=1, \dots, N} \{t_i + \delta(\mathbf{x}_i, \mathbf{x})\}.$$

The Lipschitz continuity of  $\delta$  as well as the compactness of  $\overline{\Omega \times \mathcal{U}_N}$  imply the statement.  $\square$

We note that Rademacher’s theorem ensures the differentiability of  $\Phi_N$  almost everywhere. Non-differentiability with respect to  $\mathbf{x}$  occurs for instance at  $\mathbf{x} = \mathbf{x}_i$ , but also in the presence of front collisions. An immediate consequence of this lemma is the following

**Theorem 1** (Existence). *If  $\mathcal{J}$  is uniformly continuous, then the problem (7) admits at least one minimum.*

*Proof.* The previous lemma and the uniform continuity of  $\mathcal{J}$  imply the existence of at least one minimum.  $\square$

**Proposition 1.** *Under the hypotheses of Theorem 1,  $m_N$  is a non-increasing function of  $N$ . Moreover, if there exists  $N$  such that  $m_{N+1} = m_N$ , then  $m_{N+n} = m_N$  for all  $n \geq 1$ .*

*Proof.* The first claim immediately follows from the definition of  $m_N$  and set inclusion arguments. To prove the second claim, we assume that  $m_{N+1} = m_N$  for some  $N$  and  $m_{N+2} < m_{N+1}$ . However, the choice  $\mathbf{x}_{N+1} = \mathbf{x}_{N+2}$  and  $t_{N+1} = t_{N+2}$  results in a contradiction.  $\square$

**Corollary 1.** *If  $N$  is bounded from above by  $N_{\max}$ , then  $\min_{N \leq N_{\max}} m_N$  has at least one minimum.*

**Remark 1.** 1. *From a practical point of view, this corollary ensures that by adding new EASs, we either improve the objective function or we keep the same level of accuracy. This is also seen in the experiments in Section 5, where coalescence of two or more sites is observed if introducing too many EASs.*

2. *The minimum in (7) is in general not unique as it depends on the choice of  $\mathcal{J}$  and on the order of the EASs. In principle, by permuting EASs we obtain the same value of the minimum. In particular, this symmetry induces a periodic partition of the set  $\mathcal{U}_N$ . Each partition is associated with a specific choice of the order of the EASs. From a numerical point of view, this may constitute a problem for methods based on random sampling. For deterministic steepest descent algorithms, the problem is mitigated by the fact that we rarely cross the boundary between two partitions, e.g., by swapping points, unless the two points coincide.*

3. *In general, we cannot take  $N$  unbounded with no further hypotheses on  $\mathcal{J}$ . Suppose for instance that  $\mathcal{J}$  is minimized by  $\phi(\mathbf{x}) = c$  for some constant  $c \in \mathbb{R}$ . Then,  $\inf_{N \in \mathbb{N}} m_N$  attains no minimum. Indeed, we cannot represent a constant function with (2) if  $\mathcal{E}$  is only countable. However, we can approximate the constant with arbitrary precision with a sufficiently large number  $N$  of EASs.*

## 2.3 Exponential Map

In what follows, we compute the Riemannian exponential map to derive an expression for the variation of the distance function. In particular, we discuss the relation of the derivatives of  $\Phi_N$  and the geodesic path.

We briefly recall fundamental concepts in Riemannian geometry. Given  $\mathbf{x} \in \Omega$  and a tangent vector  $\mathbf{v} \in \mathcal{V}$  for a sufficiently small neighborhood  $\mathcal{V}$  around the origin of the tangent space at  $\mathbf{x}$ , the exponential map  $\text{Exp}_{\mathbf{x}} : \mathcal{V} \rightarrow \Omega$  is given by  $\text{Exp}_{\mathbf{x}}(\mathbf{v}) = \gamma(1)$ , where  $\gamma \in C^{0,1}([0, 1], \Omega)$  is a geodesic path with  $\mathbf{v} := \dot{\gamma}(0)$ . The logarithmic map  $\text{Log}_{\mathbf{x}} : \Omega \rightarrow \mathcal{V}$  is the inverse of the exponential map  $\text{Exp}_{\mathbf{x}}^{-1}$ . In other words, the logarithmic map of  $\mathbf{y} \in \Omega$  identifies the tangent vector  $\dot{\gamma}(0)$  of a geodesic path  $\gamma$  emanating from  $\mathbf{x}$  and ending at  $\mathbf{y}$ .

**Proposition 2** (Variation of the distance function). *Let  $\mathbf{x}, \mathbf{y} \in \mathcal{V}$ , where  $\mathcal{V} \subset \hat{\Omega}$  is sufficiently small such that all points inside are connected by unique geodesics. Then the variation of  $\delta(\mathbf{x}, \mathbf{y})$  with respect to  $\mathbf{y}$  with  $\mathbf{w} = \text{Log}_{\mathbf{x}}(\mathbf{y})$  reads as*

$$\nabla_{\mathbf{x}} \delta(\mathbf{x}, \mathbf{y}) = - \frac{\mathbf{D}^{-1}(\mathbf{y}) \mathbf{w}}{\|\mathbf{w}\|_{\mathbf{D}^{-1}(\mathbf{y})}}. \quad (9)$$

*Proof.* Suppose that  $\gamma$  is a geodesic with respect to the Riemannian metric in (5) realizing the distance  $\delta(\mathbf{y}, \mathbf{x})$ , i.e.  $\gamma(0) = \mathbf{y}$ ,  $\gamma(1) = \mathbf{x}$  and

$$\delta(\mathbf{x}, \mathbf{y}) = \int_0^1 \|\dot{\gamma}(t)\|_{\mathbf{D}^{-1}(\gamma(t))} dt.$$

Let  $\tilde{\gamma} : [0, 1] \times (-R, R) \rightarrow \mathring{\Omega}$  for small  $R > 0$  be a smooth variation of  $\gamma$  such that  $\tilde{\gamma}(t, 0) = \gamma(t)$  for all  $t \in [0, 1]$ . The first variation formula [31, Chapter 10] with  $c = \|\dot{\gamma}(t)\|_{\mathbf{D}^{-1}(\gamma(t))}$  for  $t \in [0, 1]$  implies

$$\begin{aligned} \nabla_{\mathbf{x}} \delta(\mathbf{x}, \mathbf{y})(\tilde{\gamma}) &= \frac{1}{c} \left( - \int_0^1 \langle \ddot{\tilde{\gamma}}(t), \partial_2 \tilde{\gamma}(t, 0) \rangle_{\gamma(t)} dt - \sum_{i=1}^k \langle \Delta \dot{\gamma}(t_i), \partial_2 \tilde{\gamma}(t_i, 0) \rangle_{\gamma(t_i)} \right. \\ &\quad \left. + \langle \dot{\gamma}(1), \partial_2 \tilde{\gamma}(1, 0) \rangle_{\gamma(1)} - \langle \dot{\gamma}(0), \partial_2 \tilde{\gamma}(0, 0) \rangle_{\gamma(0)} \right). \end{aligned} \quad (10)$$

Here,  $0 < t_1 < \dots < t_k < 1$  are possible discontinuities of the geodesic curve and  $\Delta \dot{\gamma}(t_i) = \dot{\gamma}(t_i^+) - \dot{\gamma}(t_i^-)$ , where  $\dot{\gamma}(t_i^-)$  and  $\dot{\gamma}(t_i^+)$  denote the one-sided derivatives from the left and the right, respectively. The derivative of  $\tilde{\gamma}$  with respect to the second argument is denoted by  $\partial_2 \tilde{\gamma}$ . Since  $\gamma$  is assumed to be geodesic and smooth, the first two summands in (10) vanish.

By adjusting  $\tilde{\gamma}$  such that  $\partial_2 \tilde{\gamma}(1, 0) = 0$  and observing that  $\dot{\gamma}(0) = \text{Log}_{\mathbf{x}}(\mathbf{y})$  we have proven

$$\nabla_{\mathbf{x}} \delta(\mathbf{x}, \mathbf{y})(\tilde{\gamma}) = - \frac{\mathbf{D}^{-1}(\gamma(0)) \dot{\gamma}(0)}{\|\dot{\gamma}(0)\|_{\mathbf{D}^{-1}(\gamma(0))}} \cdot \partial_2 \tilde{\gamma}(0, 0),$$

which readily implies (9).  $\square$

In Proposition 2, we assumed uniqueness and smoothness of the geodesic curve, which is in general not ensured. In practice, the influence of geodesics violating these assumptions is negligible and thus in GEASI only consider (9) for all computations.

As before, let  $\phi_{\mathcal{E}}$  be the solution of the eikonal equation with given  $\mathcal{E} = \{(\mathbf{x}_i, t_i)_{i=1}^N\}$ . We define the region of influence as  $\mathcal{R}_i := \{\mathbf{x} \in \bar{\Omega} : \phi_{\mathcal{E}}(\mathbf{x}) = t_i + \delta(\mathbf{x}, \mathbf{x}_i)\}$ . Furthermore, the derivatives of  $\Phi_N$  with respect to  $\mathbf{x}_i$  and  $t_i$  at  $\mathbf{x} \in \mathcal{R}_i$  read as

$$\begin{aligned} \nabla_{\mathbf{x}_i} \Phi_N(\mathbf{x}, \mathbf{x}_1, \dots, \mathbf{x}_N, t_1, \dots, t_N) &= \nabla_{\mathbf{x}_i} \delta(\mathbf{x}_i, \mathbf{x}), \\ \partial_{t_i} \Phi_N(\mathbf{x}, \mathbf{x}_1, \dots, \mathbf{x}_N, t_1, \dots, t_N) &= 1, \end{aligned}$$

where we note that function is not differentiable on the boundary of the regions of interest. To compute the exponential map, we solve for each  $i = 1, \dots, N$  the following initial value problem

$$\begin{cases} \dot{\gamma}_i(t) = -\mathbf{D}(\gamma_i(t)) \nabla \phi_{\{(\mathbf{x}_i, t_i)\}}(\gamma_i(t)), \\ \gamma_i(0) = \mathbf{x} \end{cases} \quad (11)$$

for  $\mathbf{x} \in \Omega$ . The regularity and boundedness of  $\mathbf{D}$  and  $\phi_{\{(\mathbf{x}_i, t_i)\}}$  already imply the existence of solutions. Then, we define the piecewise geodesic path  $\gamma$  as  $\gamma(t) = \gamma_i(t)$  if  $\gamma(t) \in \mathcal{R}_i$ . Furthermore,

$$\bar{t} = \arg \min_{t > 0} \{\gamma(t) \in \bar{B}_{\zeta}(\mathbf{x}_i) \text{ for } i = 1, \dots, N\} \quad (12)$$

is finite due to the assumptions regarding  $\mathbf{D}$  for a small  $\zeta > 0$ . The inclusion of the  $\zeta$ -balls essentially circumvent problems related to the non-differentiability of  $\gamma_i$  in the proximity of  $(\mathbf{x}_i, t_i)$ .

We note that by construction  $\gamma$  is a unit-speed geodesic for the length functional (4). In this case, we define the exponential map in the direction  $\bar{t} \dot{\gamma}(0)$  as  $\text{Exp}_{\mathbf{x}}(\bar{t} \dot{\gamma}(0)) = \gamma(\bar{t})$ , and the logarithm  $\text{Log}_{\mathbf{x}}(\gamma(\bar{t})) = \bar{t} \dot{\gamma}(0)$  as its inverse. Note the the logarithm can efficiently be computed by tracking backward the geodesic from  $\gamma(\bar{t})$  to  $\mathbf{x}$ .

**Remark 2.** We note that points can belong to multiple regions of influence, at which the derivative of  $\phi_{\mathcal{E}}$  might not be defined. However, due to the general functional-analytic setting the Lebesgue measure of these points is negligible.

## 2.4 GEASI Algorithm

In this section, we introduce the GEASI Algorithm to solve (7) using a gradient-based approach. Here, we restrict to the specific functional

$$\mathcal{J}(\phi) := \int_{\Gamma} \frac{1}{2} (\phi(\mathbf{x}) - \hat{\phi}(\mathbf{x}))^2 d\mathbf{x},$$

where  $\Gamma \subset \Omega$  is a subdomain of  $\Omega$  with a positive Lebesgue measure and  $\widehat{\phi} \in L^2(\Gamma, \mathbb{R})$  is a fixed square-integrable function. In numerical experiments,  $\widehat{\phi}$  reflects the measurements on a known subdomain  $\Gamma$ , for which the quadratic mismatch on  $\Gamma$  between  $\phi$  and  $\widehat{\phi}$  with respect to the EASs is minimized. Examples of  $\Gamma$  include finite sets of points mimicking a contact recording map, the full endocardium/epicardium, or subregions of them.

According to Sections 2.2 and 2.3, the optimization problem for  $N = 1$  simply reads

$$\min_{(\mathbf{x}_1, t_1) \in \mathcal{U}_1} \int_{\Gamma} \frac{1}{2} (t_1 + \delta(\mathbf{x}_1, \mathbf{x}) - \widehat{\phi}(\mathbf{x}))^2 d\mathbf{x}. \quad (13)$$

To employ a gradient-based approach, we see that following Proposition 2 the gradient of  $\mathcal{J}$  with respect to  $\mathbf{x}_1$  simply reads as

$$\nabla_{\mathbf{x}_1} \mathcal{J}(\phi_{\{(\mathbf{x}_1, t_1)\}}) = - \int_{\Gamma} r(\mathbf{x}, \mathbf{x}_1, t_1) \frac{\mathbf{D}^{-1}(\mathbf{x}_1) \dot{\gamma}_{\mathbf{x}_1 \rightarrow \mathbf{x}}(0)}{\|\dot{\gamma}_{\mathbf{x}_1 \rightarrow \mathbf{x}}(0)\|_{\mathbf{D}^{-1}(\mathbf{x}_1)}} d\mathbf{x}, \quad (14)$$

where  $\gamma_{\mathbf{x}_1 \rightarrow \mathbf{x}}(t)$  is the geodesic path from  $\mathbf{x}_1$  to  $\mathbf{x}$  and  $r(\mathbf{x}, \mathbf{x}_1, t_1) = t_1 + \delta(\mathbf{x}_1, \mathbf{x}) - \widehat{\phi}(\mathbf{x})$  is the residual. Optimizing multiple points simultaneously yields an average direction weighted by the residuals  $r$  on  $\Gamma$ . Figure 2 depicts how the velocity field shown in Figure 1 translates to a descent direction to optimize (13).

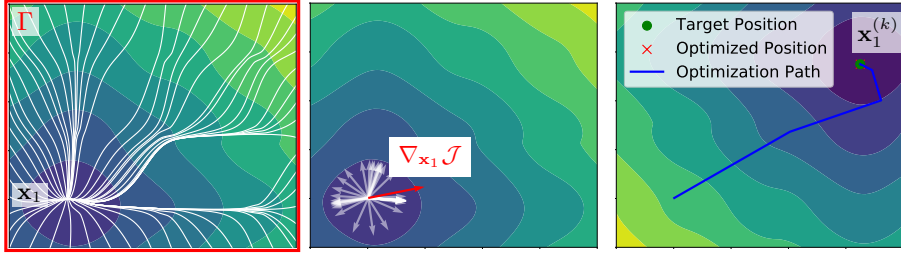


Figure 2: Visualization of the optimization problem in (13). Geodesics (white) originating from the single EAS  $\mathbf{x}_1$  to distinct points on  $\Gamma$  (left) and corresponding gradients computed with (9) (middle). The highlighted direction (red) coincides with the gradient in (14). Right: by iteratively applying a gradient-based scheme we determine the optimal  $(\mathbf{x}_1, t_1)$ .

The extension to multiple EASs works similarly. A convenient formulation consists in splitting  $\Gamma$  into subdomains  $\Gamma_i := \mathcal{R}_i \cap \Gamma$ , each composed of those points activated by the EAS  $\mathbf{x}_i$  (note that the set of points belonging to multiple regions  $\Gamma_i$  has Lebesgue measure 0). Then, the objective function reads as follows

$$\min_{\{(\mathbf{x}_i, t_i)_{i=1}^N\} \in \overline{\mathcal{U}}_N} \sum_{i=1}^N \int_{\Gamma_i} \frac{1}{2} (t_i + \delta(\mathbf{x}_i, \mathbf{x}) - \widehat{\phi}(\mathbf{x}))^2 d\mathbf{x}. \quad (15)$$

Clearly, the optimization procedure for a single EAS readily translates to the case of multiple sites.

We found that rather than a simple gradient descent scheme, a Gauss–Newton optimization proved beneficial to reduce the overall number of required optimization iterations, resulting in the following update rule

$$\mathcal{E}^{(k+1)} = \arg \min_{\{(\mathbf{x}_i, t_i)_{i=1}^N\} \in \overline{\mathcal{U}}_N} \sum_{i=1}^N \frac{1}{2} \left\| \nabla_{\mathbf{x}_i, t_i} \mathcal{J}(\phi_{\mathcal{E}^{(k)}}) \begin{pmatrix} \mathbf{x}_i - \mathbf{x}_i^{(k)} \\ t_i - t_i^{(k)} \end{pmatrix} + \phi_{\mathcal{E}^{(k)}}(\mathbf{x}) - \widehat{\phi}(\mathbf{x}) \right\|_{L^2(\Gamma)}^2. \quad (16)$$

Here,  $\mathcal{E}^{(k)} = \{(\mathbf{x}_i^{(k)}, t_i^{(k)})_{i=1}^N\}$  are the solutions of the previous iteration. To overcome local minima of the optimization problem (7) caused by non-unique solutions (see Remark 1) we additionally use an over-relaxation [9] with fixed  $\beta_a = \frac{1}{\sqrt{2}}$ . The resulting Algorithm 1 iteratively linearizes and solves the problem using the computed gradient from  $\delta$  to match a given measured activation. We remark that the gradient properly reflects infinitesimal changes of activation times on  $\mathcal{R}_i$  for

each  $\mathbf{x}_i$ , but it is not capable of accurately capturing higher order effects like the change of  $\mathcal{R}_i$ . The experiments showed that rather than directly using  $\mathcal{E}^{(k+1)}$  from (16) as the new solution, it is beneficial to take a step-size  $\beta_s < 1$  and compute the convex combination of old and new solution according to this step size. For all experiments, we used  $\beta_s = \frac{1}{2}$ . For further details of the numerical realization we refer the reader to Section 4.

**Algorithm 1: GEASI**

**Input** : initial  $\mathbf{x}_i^{(0)}$  and  $t_i^{(0)}$  defining  $\mathcal{E}^{(0)} = \{(\mathbf{x}_i^{(0)}, t_i^{(0)})_{i=1}^N\}$ ,  
target activation  $\hat{\phi}(\mathbf{x})$  for  $\mathbf{x} \in \Gamma$ , conduction velocity tensor  $\mathbf{D}$   
**Output**: optimal EASs  $\mathbf{x}_i^*$  and times  $t_i^*$   
**for**  $k = 1, \dots, K$  **do**  
     $\tilde{\mathcal{E}}^{(k)} = \mathcal{E}^{(k)} + \beta_a(\mathcal{E}^{(k)} - \mathcal{E}^{(k-1)})$   
    solve the eikonal equation (1) for  $\tilde{\mathcal{E}}^{(k)} = \{(\tilde{\mathbf{x}}_i^{(k)}, \tilde{t}_i^{(k)})_{i=1}^N\}$   
    compute all geodesics  $\gamma_{\mathbf{x}_i \rightarrow \mathbf{x}}(t)$  for  $\mathbf{x} \in \Gamma$  by solving (11)  
    compute  $\bar{\mathcal{E}}^{(k+1)}$  using (16) (with  $\tilde{\mathcal{E}}^{(k)}$ )  
     $\mathcal{E}^{(k+1)} = \tilde{\mathcal{E}}^{(k)} + \beta_s(\bar{\mathcal{E}}^{(k+1)} - \tilde{\mathcal{E}}^{(k)})$   
**end**

### 3 Extensions of GEASI

GEASI is a versatile optimization algorithm, which can be extended in several aspects. In this section, we focus on two such possible extensions. First, the topological gradient estimation allows for an accurate estimation of the number of EASs. Second, we modify the original objective function of GEASI to fit a given ECG.

#### 3.1 Variable number of EASs: Topological Gradient

So far, we assumed the number of EASs  $N$  to be fixed. Since the optimal number of EASs is in general unknown, we subsequently propose a method to approximate the optimal  $N$ . As a possible approach to estimate  $N$  (which is not conducted in this work) one could start with a large number and successively remove distinct EASs that violate the constraint (6). However, this approach suffers from some major drawbacks:

- several local minima can occur leading to a strong dependency on the initial guess,
- enforcing (6) results in some numerical issues, e.g. dimension changes of the optimization problem and order of EAS removal.

In contrast, starting with a few (or even a single) EASs and subsequently introducing new EASs overcomes the above issues since according to Proposition 1 adding new sites does not increase the objective functional. In what follows, we briefly recall the topological gradient, which is used to compute the infinitesimal expansion of splitting a single EAS. This expansion is exploited to estimate the energy decrease of adding a new site.

Consider the case of a single EAS, i.e.  $N = 1$ . The topological gradient is defined as the effect on the solution of the associated eikonal equation if splitting a single EAS  $\mathbf{x}_1$  into two new sites  $\mathbf{x}_1 + \varepsilon \mathbf{n}$  and  $\mathbf{x}_1 - \varepsilon \mathbf{n}$  in the direction of  $\mathbf{n} \in \mathbb{S}^{d-1}$ . We can directly infer from (2) that

$$\phi_{\mathcal{E}_\varepsilon}(\mathbf{x}) = \min\{t_1 + \delta(\mathbf{x}_1 - \varepsilon \mathbf{n}, \mathbf{x}), t_1 + \delta(\mathbf{x}_1 + \varepsilon \mathbf{n}, \mathbf{x})\}$$

for  $\mathcal{E}_\varepsilon = \{(\mathbf{x}_1 + \varepsilon \mathbf{n}, t_1), (\mathbf{x}_1 - \varepsilon \mathbf{n}, t_1)\}$ , where  $\varepsilon > 0$  is sufficiently small. This topological operation divides the domain into two subdomains  $\Omega_\varepsilon^- := \{\mathbf{x} \in \Omega : \delta(\mathbf{x}_1 - \varepsilon \mathbf{n}, \mathbf{x}) < \delta(\mathbf{x}_1 + \varepsilon \mathbf{n}, \mathbf{x})\}$  and  $\Omega_\varepsilon^+ = \Omega \setminus \Omega_\varepsilon^-$ . We can now expand  $\phi_\varepsilon$  with respect to  $\varepsilon$  as follows

$$\begin{aligned} \phi_{\mathcal{E}_\varepsilon}(\mathbf{x}) &= t_1 + \delta(\mathbf{x}_1, \mathbf{x}) + \varepsilon \min\{-\nabla_{\mathbf{x}_1} \delta(\mathbf{x}_1, \mathbf{x}) \cdot \mathbf{n}, \nabla_{\mathbf{x}_1} \delta(\mathbf{x}_1, \mathbf{x}) \cdot \mathbf{n}\} + o(\varepsilon) \\ &= \Phi_1(\mathbf{x}, \mathbf{x}_1, t_1) - \varepsilon |\nabla_{\mathbf{x}_1} \delta(\mathbf{x}_1, \mathbf{x}) \cdot \mathbf{n}| + o(\varepsilon), \end{aligned}$$

where  $\Phi_1$  was defined in (8) and we used (9). In this case, we call the quantity

$$j(\mathbf{x}, \mathbf{x}_1, \mathbf{n}) := |\nabla_{\mathbf{x}_1} \delta(\mathbf{x}_1, \mathbf{x}) \cdot \mathbf{n}|. \quad (17)$$

the *topological gradient*. A visual example of the topological gradient is provided in Figure 3. We note that adding new optimal sites always decreases the objective functional unless  $\nabla_{\mathbf{x}_1} \delta(\mathbf{x}_1, \mathbf{x}) \cdot \mathbf{n} = 0$ . Therefore, we shall define a criterion for adding a split. The decrease in energy of splitting a single site can be estimated as follows:

$$\nu_{S,\varepsilon} := \min_{\mathbf{n} \in \mathbb{S}^{d-1}} \int_{\Gamma} (\Phi_1(\mathbf{x}, \mathbf{x}_1, t_1) - \widehat{\phi}(\mathbf{x}))^2 - (\Phi_1(\mathbf{x}, \mathbf{x}_1, t_1) + \varepsilon j(\mathbf{x}, \mathbf{x}_1, \mathbf{n}) - \widehat{\phi}(\mathbf{x}))^2 dx. \quad (18)$$

Likewise, the effect of moving a source point in direction  $\mathbf{n}$  is given by

$$\begin{aligned} \nu_{M,\varepsilon} := \min_{\mathbf{n} \in \mathbb{S}^{d-1}} \int_{\Gamma} & (\Phi_1(\mathbf{x}, \mathbf{x}_1, t_1) - \widehat{\phi}(\mathbf{x}))^2 \\ & - (\Phi_1(\mathbf{x}, \mathbf{x}_1, t_1) + \varepsilon \nabla_{\mathbf{x}_1} \delta(\mathbf{x}_1, \mathbf{x}) \cdot \mathbf{n} - \widehat{\phi}(\mathbf{x}))^2 dx. \end{aligned}$$

The ratio  $\frac{\nu_{M,\varepsilon}}{\nu_{S,\varepsilon}}$  has proven to be a robust score for adding new sites, which is verified in the numerical experiments. In particular, if the ratio is below a certain threshold, then a new EAS is introduced.

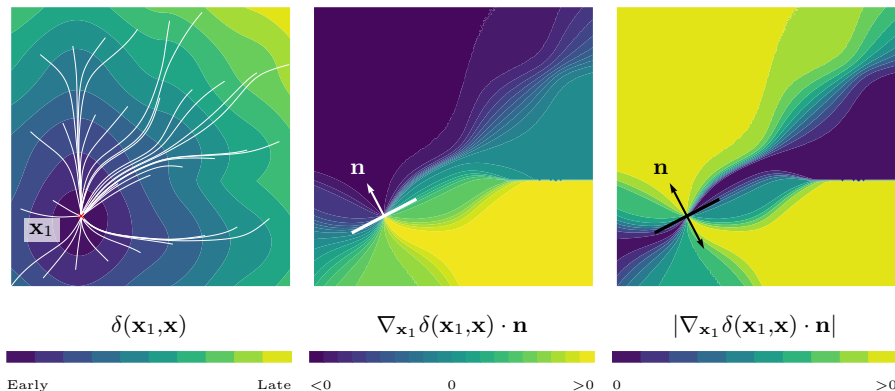


Figure 3: Left: geodesics (white) joining multiple points with  $\mathbf{x}_1$ . Contour plots of  $\mathbf{x} \mapsto \nabla_{\mathbf{x}_1} \delta(\mathbf{x}_1, \mathbf{x}) \cdot \mathbf{n}$  (middle) and  $\mathbf{x} \mapsto j(\mathbf{x}, \mathbf{x}_1, \mathbf{n})$  (right) for fixed  $\mathbf{n} \in \mathbb{S}^{d-1}$ . Moving a single EAS in the direction  $\mathbf{n}$  alters the activation times  $\delta(\mathbf{x}_1, \mathbf{x})$  as shown. In contrast, splitting in the same direction  $\mathbf{n}$  is similar to simultaneously moving a source point in both directions, and keeping only the shorter geodesic (right).

### 3.2 Optimization using the ECG

The electrocardiogram (ECG) is the observed signature of the electric activity of the heart, which is measured at selected locations on the chest. Being routinely acquired and non-invasive, the ECG is the ideal candidate for inferring cardiac activation in a clinical framework. Here, we will introduce a method to reconstruct the EASs directly from ECG measurements. To this end, we exploit the methods presented in [30, 33] to efficiently compute the ECG from activation maps of the eikonal equation. Finally, the quadratic mismatch of the computed and measured ECG is minimized, which yields optimal EASs.

From a modeling perspective, we denote  $\Omega_T \subset \mathbb{R}^d \setminus \Omega$  as the whole body domain excluding the heart cavity  $\Omega \subset \mathbb{R}^d$ . The heart surface  $\Gamma := \overline{\Omega_T} \cap \overline{\Omega}$  is the interface between torso and heart, that is the boundary between the active myocardium and the rest of the body (for instance, endocardium plus epicardium). In this setting,  $\Sigma := \partial\Omega_T \setminus \Gamma$  is the chest, on which the aforementioned electrical signal is recorded. We denote by  $\mathbb{T} \subset \mathbb{R}$  the considered time interval. In Figure 4, we outline how this setup would look in actual clinical measurements on the example of Lead I.

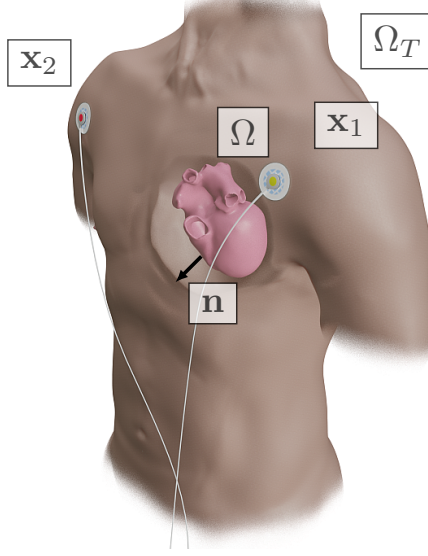


Figure 4: Exemplary setup for the lead-field of Lead I appearing in many ECG recordings.  $\Omega_T$  (torso) encapsulates heart domain  $\Omega$  (heart domain), the left/right arm electrodes on  $\Omega_T$  are marked as  $\mathbf{x}_1$  and  $\mathbf{x}_2$ . The normal  $\mathbf{n}$  is pointing from the surface of the heart domain  $\Omega$  into the torso domain  $\Omega_T$ . The corresponding  $Z_i$  is computed using (23), which is subsequently employed to obtain the ECG  $V_i$  of Lead I.

An equation for the torso potential can be derived from bidomain theory for the cardiac tissue and the balance of currents in the body (see e.g. [12]). The resulting system of equations reads as follows:

$$\left\{ \begin{array}{ll} -\nabla \cdot (\mathbf{G} \nabla u_e) = \nabla \cdot (\mathbf{G}_i \nabla V_m), & \text{in } \Omega \times \mathbb{T}, \\ -\nabla \cdot (\mathbf{G}_T \nabla u_T) = 0, & \text{in } \Omega_T \times \mathbb{T}, \\ -\mathbf{G}_T \nabla u_T \cdot \mathbf{n} = 0, & \text{in } \Sigma \times \mathbb{T}, \\ u_e(\mathbf{x}^-, t) = u_T(\mathbf{x}^+, t), & (\mathbf{x}, t) \in \Gamma \times \mathbb{T}, \\ \mathbf{G}_T(\mathbf{x}^+) \nabla u_T(\mathbf{x}^+, t) \cdot \mathbf{n} \\ -\mathbf{G}(\mathbf{x}^-) \nabla u_e(\mathbf{x}^-, t) \cdot \mathbf{n} = \mathbf{G}_i(\mathbf{x}^-) \nabla V_m(\mathbf{x}^-, t) \cdot \mathbf{n}, & (\mathbf{x}, t) \in \Gamma \times \mathbb{T}, \end{array} \right. \quad (19)$$

where the following quantities occur:

- $u_e: \Omega \times \mathbb{T} \rightarrow \mathbb{R}$  is the extracellular potential in the heart,
- $V_m: \Omega \times \mathbb{T} \rightarrow \mathbb{R}$  is the transmembrane potential,
- $u_T: \Omega_T \times \mathbb{T} \rightarrow \mathbb{R}$  is the potential in the torso,
- $\mathbf{G}_T: \Omega_T \rightarrow \text{Sym}^{d \times d}$  is the electric conductivity of the torso,
- $\mathbf{G}_i: \Omega \rightarrow \text{Sym}^{d \times d}$  is the intracellular conductivity,
- $\mathbf{G}_e: \Omega \rightarrow \text{Sym}^{d \times d}$  is the extracellular conductivity, and
- $\mathbf{G} = \mathbf{G}_i + \mathbf{G}_e$  is the bulk conductivity of the heart.

The normal vector  $\mathbf{n}$  at  $\mathbf{x} \in \Gamma$  points outwards, i.e. from the heart surface towards the torso, and is the outer normal vector for  $\mathbf{x} \in \Sigma$ . The points  $\mathbf{x}^\pm$  associated with  $\mathbf{x} \in \Gamma$  are obtained by taking the limit  $\mathbf{x}_\varepsilon^\pm = \mathbf{x} \pm \varepsilon \mathbf{n}$  for  $\varepsilon \rightarrow 0$ .

The well-posedness of (19) follows from standard arguments for elliptic PDEs (see [22]). However, some care is required for the discontinuity across the heart-torso interface  $\Gamma$ . Indeed, in order to render (21) meaningful, we need at least  $u_T$  to be continuous on  $\Sigma$  for every  $t \in \mathbb{T}$ . Let

$\tilde{\Omega} = \Omega \cup \Omega_T \cup \Gamma$  be the domain modeling the whole torso (including the heart), and

$$\tilde{\mathbf{G}} = \begin{cases} \mathbf{G}, & \text{in } \Omega, \\ \mathbf{G}_T, & \text{in } \Omega_T, \end{cases} \quad \tilde{u} = \begin{cases} u_e, & \text{in } \Omega \times \mathbb{T}, \\ u_T, & \text{in } \Omega_T \times \mathbb{T}. \end{cases}$$

Following [12], we assume that

1.  $\Omega, \Omega_T \subset \mathbb{R}^d$  are Lipschitz domains,
2.  $\mathbf{G}_i, \mathbf{G}_e \in C^1(\Omega, \text{Sym}^{d \times d})$  and  $\tilde{\mathbf{G}} \in L^\infty(\tilde{\Omega}, \text{Sym}^{d \times d})$ ,
3.  $V_m(\cdot, t) \in W^{2,p}(\Omega)$  for all  $t \in \mathbb{T}$  with  $p > d$ .

**Proposition 3.** *Under the above assumptions, the weak formulation of (19) given by*

$$\text{find } \tilde{u} \in H^1(\tilde{\Omega}) \text{ s.t. } \int_{\tilde{\Omega}} \tilde{\mathbf{G}} \nabla \tilde{u} \cdot \nabla v \, d\mathbf{x} = - \int_{\Omega} \mathbf{G}_i \nabla V_m \cdot \nabla v \, d\mathbf{x} \quad \forall v \in H^1(\tilde{\Omega}) \quad (20)$$

is well-defined. In particular, there exists a unique solution up to an additive constant (the reference potential).

The proof directly follows from the Lax–Milgram theorem [22] by noting that  $V_m(\cdot, t) \in W^{2,p}(\Omega)$  and  $\tilde{u}(\cdot, t) \in W^{1,p}(\tilde{\Omega})$  for  $p > d$  and all  $t \in \mathbb{T}$ .

Let  $\mathbf{x}_e \in \Sigma$ ,  $e = 1, \dots, N_E$ , be  $N_E$  electrodes placed on the chest. A single-lead ECG recording is the potential difference between two such electrodes or, more generally, a zero-sum linear combination of the recordings. For instance, Einthoven’s lead I is the potential difference between left and right arm electrodes. More generally, given electric potentials  $u_T$  at the electrodes, the standard ECG is a vector-valued function  $\mathbf{V}: \mathbb{T} \rightarrow \mathbb{R}^L$  given by

$$\mathbf{V}(t) = \begin{pmatrix} V_1(t) \\ V_2(t) \\ \vdots \\ V_L(t) \end{pmatrix} = \mathbf{A} \begin{pmatrix} u_T(\mathbf{x}_1, t) \\ u_T(\mathbf{x}_2, t) \\ \vdots \\ u_T(\mathbf{x}_{N_E}, t) \end{pmatrix}, \quad (21)$$

where  $L$  is the number of leads and  $\mathbf{A}$  is a  $L \times N_E$  real matrix defining the lead system, e.g. the 12-lead ECG. Since each row of  $\mathbf{A}$  sums to zero, the matrix is not full-rank. For instance, the standard 12-lead ECG corresponds to the choice  $L = 12$  (3 Einthoven leads, 3 augmented limb leads and 6 precordial leads) and  $N_E = 9$  (3 limb electrodes and 6 precordial electrodes), in which case  $\mathbf{A}$  has rank 8. We remark that Morrey’s inequality guarantees  $\tilde{u}(\cdot, t) \in C^0(\tilde{\Omega})$ , hence validating (21).

Solving (19) is numerically costly for the standard 12-lead ECG, since we only evaluate  $u_T$  at selected locations. Note that the system must be solved for every  $t \in \mathbb{T}$ . Thus, we adopt the following integral representation of the (21):

$$V_l(t) = \int_{\Omega} \mathbf{G}_i(\mathbf{x}) \nabla V_m(\mathbf{x}, t) \cdot \nabla Z_l(\mathbf{x}) \, d\mathbf{x}, \quad (22)$$

where  $Z_l: \tilde{\Omega} \rightarrow \mathbb{R}$  are the lead fields (or Green’s functions) satisfying the adjoint problem

$$\begin{cases} -\nabla \cdot (\tilde{\mathbf{G}} \nabla Z_l) = 0, & \text{in } \tilde{\Omega}, \\ \mathbf{G}_T \nabla Z_l(\mathbf{x}) = - \sum_{e=1}^{N_E} [\mathbf{A}]_{le} \delta_{[\mathbf{x}-\mathbf{x}_e]}, & \mathbf{x} \in \Sigma, \\ Z_l(\mathbf{x}^-) = Z_l(\mathbf{x}^+), & \mathbf{x} \in \Gamma, \\ \mathbf{G}_T \nabla Z_l(\mathbf{x}^+) \cdot \mathbf{n} = \mathbf{G} \nabla Z_l(\mathbf{x}^-) \cdot \mathbf{n}, & \mathbf{x} \in \Gamma. \end{cases} \quad (23)$$

An informal derivation of (22) follows from the application of the second Green’s identity to (19). For a rigorous derivation accounting for the discontinuity in  $\tilde{\mathbf{G}}$ , we refer the reader to [12, pp. 152 ff.].



Next, we compute the torso potential  $u_T$  in (19) from the solution of the anisotropic eikonal equation (1). To this end, we assign the transmembrane potential  $\widetilde{V}_m$  accordingly to a fixed waveform  $U: \mathbb{R} \rightarrow \mathbb{R}$  shifted by the activation time  $\phi_{\mathcal{E}}$  as follows

$$\widetilde{V}_m(\mathbf{x}, t, \mathcal{E}) = U(t - \phi_{\mathcal{E}}(\mathbf{x})).$$

We write the parametrized waveform as:

$$U(\xi) = K_0 + \frac{K_1 - K_0}{2} \left[ \tanh\left(2\frac{\xi}{\tau_1}\right) - \tanh\left(2\frac{\xi - \text{APD}}{\tau_2}\right) \right], \quad (24)$$

which is visualized in Figure 5.

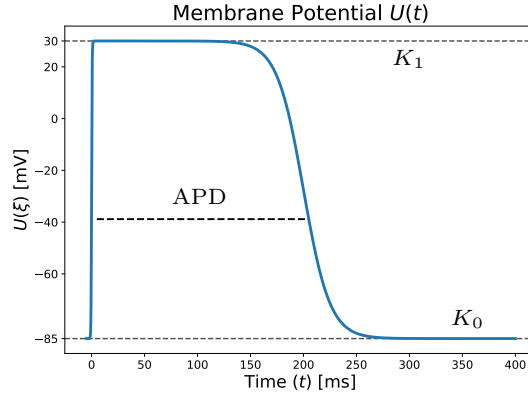


Figure 5: Membrane voltage waveform as a function of time, equivalent to (24) with parameters from Table 1. The continuous formulation allows for an analytical derivation in (25).

Parameter	Description	Value	Unit
$t$	time	$[0, T]$	ms
$\lambda$	equal anisotropy ratio	3	
$\mathbf{G}_T$	torso conductivity	0.2	$\frac{\text{mS}}{\text{mm}}$
$\alpha$	conduction velocity scaling	20	$\text{mm}(\text{ms mS}^{-1/2})^{-1}$
$\beta$	surface-to-volume ratio	$10^3$	$\text{mm}^{-1}$
$K_0$	resting potential	-85	mV
$K_1$	plateau potential	30	mV
$\tau_1$	depolarization time-scale	1	ms
$\tau_2$	repolarization time-scale	50	ms
APD	action potential duration	200	ms

Table 1: Parameters to compute the ECG from the eikonal solution  $\phi_{\mathcal{E}}$ .

Furthermore, the conduction velocity tensor  $\mathbf{D}$  in the anisotropic eikonal equation in (1) is linked to the electric conductivity as follows:

$$\mathbf{D} = \frac{\alpha^2}{\beta} \mathbf{G}_e \mathbf{G}^{-1} \mathbf{G}_i,$$

where  $\beta$  is the surface-to-volume ratio and  $\alpha$  is a rescaling factor either experimentally estimated or obtained by solving the monodomain equation in a cable propagation setup [33]. Note that in all conducted experiments we assumed an equal anisotropy ratio  $\mathbf{G}_i = \lambda \mathbf{G}_e$ , from which  $\mathbf{D} = \frac{\alpha^2}{\beta} \frac{\lambda}{1+\lambda} \mathbf{G}_i$  follows. All parameters adopted in this study are provided in Table 1.

We emphasize that  $\phi_{\mathcal{E}} \in C^{0,1}(\overline{\Omega})$  only implies  $\widetilde{V}_m(\cdot, t, \mathcal{E}) \in W^{1,p}(\Omega)$  and not  $\widetilde{V}_m(\cdot, t, \mathcal{E}) \in W^{2,p}(\Omega)$  as required for  $t \in \mathbb{T}$  and  $\mathcal{E} \in \mathcal{U}_N$ . However, the aforementioned theory is still valid in

this case with some major modifications that are beyond the scope of this work. Again, we refer to [12] and the references therein for further details.

In what follows, we intend to compute the sensitivities of the ECG with respect to the parameter set  $\mathcal{E} \in \mathcal{U}_N$ . In the problem, only the activation map  $\phi_{\mathcal{E}}$  appearing in the definition of  $\widetilde{V}_m$  depends on the parameters in  $\mathcal{E}$ . Note that the chain rule straightforwardly implies

$$\nabla_{\mathcal{E}} \widetilde{V}_m = -\frac{\partial U}{\partial \xi} \nabla_{\mathcal{E}} \phi_{\mathcal{E}}.$$

The use of the aforementioned smooth waveform allows for a continuous analytical derivative  $\frac{\partial U}{\partial \xi}$ . Details on the derivation of the term  $\nabla_{\mathcal{E}} \phi_{\mathcal{E}}$  were already given in Section 2.3. Then, the derivative  $\nabla_{\mathcal{E}} V_l$  is computed from (22) and reads as

$$\nabla_{\mathcal{E}} V_l(t, \mathcal{E}) = \int_{\Omega} \left( \mathbf{G}_i(\mathbf{x}) \nabla_{\mathcal{E}, \mathbf{x}}^2 \widetilde{V}_m(\mathbf{x}, t, \mathcal{E}) \right) \nabla Z_l(\mathbf{x}) \, d\mathbf{x}. \quad (25)$$

Finally, in this model the set of EASs  $\mathcal{E}$  is computed from the measured ECG  $\widehat{V}_l : I \rightarrow \mathbb{R}$  as follows:

$$\min_{\mathcal{E} \in \mathcal{U}_N} \frac{1}{2} \sum_{l=1}^L \int_{\mathbb{T}} \left( V_l(t, \mathcal{E}) - \widehat{V}_l(t) \right)^2 \, dt, \quad (26)$$

which is solved using the Gauss–Newton algorithm in a similar fashion to Algorithm 1. In particular, the update of the set  $\mathcal{E}$  reads as follows

$$\begin{aligned} \mathcal{E}^{(k+1)} = & \arg \min_{\{(\mathbf{x}_i, t_i)_{i=1}^N\} \in \overline{\mathcal{U}_N}} \\ & \sum_{l=1}^L \sum_{i=1}^N \frac{1}{2} \left\| \nabla_{\mathbf{x}_i, t_i} \mathcal{J}(\mathcal{E}^{(k)}) (\mathbf{x}_i - \mathbf{x}_i^{(k)}, t_i - t_i^{(k)})^{\top} + V_l(t, \mathcal{E}^{(k)}) - \widehat{V}_l(t) \right\|_{L^2(\mathbb{T})}^2 \end{aligned} \quad (27)$$

with the modified objective functional

$$\mathcal{J}(\mathcal{E}) = \frac{1}{2} \sum_{l=1}^L \int_{\mathbb{T}} \left( V_l(t, \mathcal{E}) - \widehat{V}_l(t) \right)^2 \, dt.$$

The numerical integration in (27) is realized using the trapezoidal rule.

**Remark 3.** *There are several numerical issues related to the optimization:*

1. *The waveform (24) is a rough approximation of a physiological action potential modelled the electrophysiology of a cell. The function  $U$  and the scaling parameter  $\alpha$  may be simultaneously approximated from a generic ionic model by solving a 1-D propagation in a (possibly very long) cable with uniform coefficients. Alternatively, it is possible to show that  $(U, U', \alpha)$  solves a nonlinear eigenvalue problem involving the ionic model [26].*
2. *The approximation  $\widetilde{V}_m$  is not suitable to model the repolarization of the heart which is responsible for the T-wave. The reason is that the polarity of the T-wave, in general in accordance with the polarity of the QRS complex, can only arise from a heterogeneity in the action potential. Such heterogeneity might be introduced here, but it would be hard to reproduce the smoothing effect due to diffusion currents. Finally, the eikonal model is not suitable for the repolarization because, opposed to the depolarization phase, the repolarization front is of the same order of the size of the domain, impeding a proper perturbation analysis. In this work, the repolarization time is  $\phi_{\mathcal{E}}(\mathbf{x}) + \text{APD}$ , hence it satisfies the same equation as  $\phi_{\mathcal{E}}$ , but with a shifted time.*
3. *Equation (25) requires higher order derivatives of  $\widetilde{V}_m$  and subsequently  $\phi_{\mathcal{E}}$ . While we computed the derivative  $\nabla_{\mathcal{E}} \widetilde{V}_m$  as previously discussed, the computation of  $\nabla_{\mathbf{x}} \widetilde{V}_m$  is numerically achieved on the reference element.*

4. It is important to mention that the gradient computation for the minimization of (26) is usually much more costly compared to optimizing the problem in the eikonal formulation from (13), since the size of  $\Gamma$  is much smaller compared to  $\Omega$ . However, to compute  $\nabla_{\mathbf{x}_i, t_i} \mathcal{J}$  we need the activation times and their derivatives in  $\Omega$ , which necessitates the computation of the geodesics from each point of our domain to the EAS  $\mathbf{x}_i$ . The computational complexity is significantly larger than the complexity for (13). Further strategies to reduce additional computational costs are presented in Section 6.2.

## 4 Discretization

In this section, we elaborate on the discretization aspects for Algorithm 1, which encompasses the steps: over-relaxation of  $\mathcal{E}^{(k+1)}$ , solving the eikonal equation, computation of the geodesics and update of  $\mathcal{E}^{(k+1)}$ .

### 4.1 Solving the Eikonal Equation

The discrete function space for the eikonal equation is the space of volumetric Lagrange  $\mathcal{P}^1$ -finite elements defined on triangular ( $d = 2$ ) and tetrahedral ( $d = 3$ ) meshes discretizing  $\Omega$ , respectively. Moreover, the discrete measurements in  $\Gamma$  are degrees of freedom (DOFs) of the mesh.

Typically, finite element solvers require the initiation sites to coincide with DOFs of the mesh. However, since the original problem (7) expresses  $\mathbf{x}_i$  as a continuous quantity, we identify the DOFs of the actual element containing the activation site. Then, these DOFs are added to the Dirichlet boundary  $\Gamma_D$  with fixed activation times given by  $t_i + \|\mathbf{x} - \mathbf{x}_i\|_{\mathbf{D}^{-1}(\mathbf{x}_i)}$  for  $\mathbf{x} \in \Gamma_D$  due to structural assumptions regarding the  $\mathcal{P}^1$ -finite element space. For the rare case of two or more initiation sites residing in the same element, we use the properties of (2) and (6) to compute the activation times.

In all subsequent computations, we employ the FIM [19, 20] to solve the eikonal equation to account for the anisotropy.

### 4.2 Computation of Geodesics

In this work, we employ Heun's method (second order explicit Runge–Kutta scheme) to solve (11), which proved to be stable and efficient in numerical experiments. Due to the convergence of the ODE system to a stable node  $\mathbf{x}_i$  we terminate the iteration if the  $\ell^2$ -norm of two consecutive iterations is below  $10^{-10}$ . In practice, the ODE system is solved independently on each region of interest  $\mathcal{R}_i$  incorporating the whole set  $\mathcal{E}$ . Since the gradient of the eikonal solution for the chosen discretization is a  $\mathcal{P}^0$ -finite element function (i.e. piecewise constant), we advocate a standard  $L^2$ -projection onto the  $\mathcal{P}^1$ -finite element space [28]. Note that this projection can be realized by solving a linear system involving the mass matrix in  $\mathcal{P}^1$ . Since the boundary of  $\Omega$  is in general curved, we project the geodesics back onto  $\partial\Omega$  if they are outside of the domain after each update.

As remarked in Section 2.3, the gradient of the eikonal solution is discontinuous around each  $\mathbf{x}_i$ . To enforce regular gradients at each  $\mathbf{x}_i$  after the  $L^2$ -projection of the previous eikonal solution  $\tilde{\phi}_{\mathcal{E}}$ , we recompute the points with vanishing gradient by the subsequent variational problem with Tikhonov regularization for  $c \in \llbracket d \rrbracket$  and balancing parameter  $\lambda > 0$  as follows:

$$\begin{pmatrix} [\nabla\phi_{\mathcal{E}}(\mathbf{y}_1)]_c \\ \vdots \\ [\nabla\phi_{\mathcal{E}}(\mathbf{y}_{d+1})]_c \end{pmatrix} = \arg \min_{\mathbf{n} \in \mathbb{R}^{d+1}} \frac{1}{2} \langle \Psi(\mathbf{x}_i), \mathbf{n} \rangle^2 + \frac{\lambda}{2} \left\| \mathbf{n} - \begin{pmatrix} [\nabla\tilde{\phi}_{\mathcal{E}}(\mathbf{y}_1)]_c \\ \vdots \\ [\nabla\tilde{\phi}_{\mathcal{E}}(\mathbf{y}_{d+1})]_c \end{pmatrix} \right\|^2.$$

Here,  $\Psi = (\psi_1, \dots, \psi_{d+1})^\top$  and  $\{\mathbf{y}_j\}_{j=1}^{d+1}$  are the collections of  $\mathcal{P}^1$ -basis functions and degrees of freedom associated with the element containing  $\mathbf{x}_i$ , respectively. Figure 6 depicts the effect of this regularization on the solution around  $\mathbf{x}_i$ .

The gradient computation in (9) is also sensitive to the choice of the step sizes of (11), which we choose as  $5 \cdot 10^{-2}h$  with  $h$  being the average element size. As already described in Section 2.3, we compute the geodesic direction not directly at  $\mathbf{x}_i$ , but rather in a small  $\zeta$ -neighborhood with

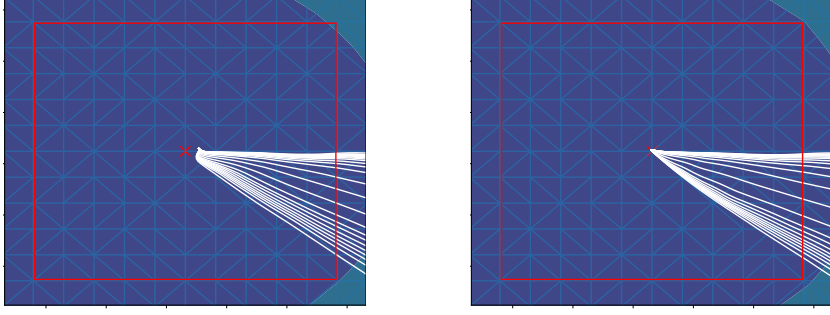


Figure 6: Left: zoom of family of geodesics emanating from a single EAS without special handling. Note that before the  $L^2$ -projection of  $\nabla\phi_{\mathcal{E}}$  geodesics are not guaranteed to reach the EAS. Right: after the  $L^2$ -projection all geodesic curves actually reach the EAS.

$\zeta = 0.5h$  as advocated in (12). Numerically, the convergence of geodesics to this neighborhood is not ensured and non-converged geodesics (rarely occurring) do not affect the optimization.

### 4.3 Update of $\mathcal{E}^{(k+1)}$

Next, we optimize (16), where we have to ensure  $\mathcal{E} \in \overline{\mathcal{U}_N}$ . The constraint  $\mathbf{x}_i \in \overline{\Omega}$  is mesh-dependant and allows for no general analytical solution, potentially limiting the available optimization implementations. To overcome this hurdle, we use a proximal point algorithm enforcing  $\mathcal{E} \in \overline{\mathcal{U}_N}$ . The integration is realized using an exact simplex quadrature rule.

In detail, we first compute the Moreau envelope of (16) with respect to the metric induced by  $\mathbf{M}_{i,\mathcal{E}^{(k)}} := \frac{1}{\tau}\mathbf{I} - \mathbf{J}_{i,\mathcal{E}^{(k)}}^\top \mathbf{J}_{i,\mathcal{E}^{(k)}}$  for  $\tau > \|\mathbf{J}_{i,\mathcal{E}^{(k)}}^\top \mathbf{J}_{i,\mathcal{E}^{(k)}}\|^{-1}$ , where  $\mathbf{J}_{i,\mathcal{E}^{(k)}} := \nabla_{(\mathbf{x}_i, t_i)} \mathcal{J}(\mathbf{x}_i^{(k)}, t_i^{(k)})$ . Thus, the Moreau envelope reads as

$$f(\overline{\mathcal{E}}) := \min_{\mathcal{E} \in \overline{\mathcal{U}_N}} \sum_{i=1}^N \frac{1}{2} \left\| \mathbf{J}_{i,\mathcal{E}^{(k)}} \begin{pmatrix} \mathbf{x}_i - \mathbf{x}_i^{(k)} \\ t_i - t_i^{(k)} \end{pmatrix} + \mathbf{r}_{\mathcal{E}^{(k)}}(\mathbf{x}) \right\|_{L^2(\Gamma)}^2 + \frac{1}{2} \left\| \begin{pmatrix} \overline{\mathbf{x}}_i - \mathbf{x}_i \\ \overline{t}_i - t_i \end{pmatrix} \right\|_{\mathbf{M}_{i,\mathcal{E}^{(k)}}}^2 \quad (28)$$

with  $\mathcal{E} = \{(\mathbf{x}_i, t_i)_{i=1}^N\}$  and  $\overline{\mathcal{E}} = \{(\overline{\mathbf{x}}_i, \overline{t}_i)_{i=1}^N\}$ , and  $\mathbf{r}_{\mathcal{E}^{(k)}}(\mathbf{x}) = \phi_{\mathcal{E}^{(k)}}(\mathbf{x}) - \widehat{\phi}(\mathbf{x})$ . This particular choice of the metric [9] allows for an explicit solution to (28) given the projection onto  $\mathcal{U}_N$ . This method is usually referred to as Iterative Shrinkage and Thresholding (ISTA, [17]). In summary, the iteration step of the proximal point algorithm reads as

$$\widehat{\mathcal{E}} = \left\{ \left( \text{proj}_{\mathcal{U}_1} \left( \begin{pmatrix} \overline{\mathbf{x}}_i \\ \overline{t}_i \end{pmatrix} - \int_{\Gamma} \tau \mathbf{J}_{i,\mathcal{E}^{(k)}}^\top \left( \mathbf{J}_{i,\mathcal{E}^{(k)}} \begin{pmatrix} \overline{\mathbf{x}}_i - \mathbf{x}_i^{(k)} \\ \overline{t}_i - t_i^{(k)} \end{pmatrix} + \mathbf{r}_{\mathcal{E}^{(k)}}(\mathbf{x}) \right) \text{d}\mathbf{x} \right) \right)_{i=1}^N \right\}.$$

Thus, the resulting optimal set is  $\widehat{\mathcal{E}} = \{(\widehat{\mathbf{x}}_i, \widehat{t}_i)_{i=1}^N\}$ . Note that the convexity of the projection depends on the convexity of the domain. In practice, hardly any cardiac mesh is convex, but nevertheless the proposed method generated reliable results for sufficiently small step sizes. The gradient direction of the Moreau-envelope is

$$\nabla_{\mathbf{x}_i, t_i} f(\overline{\mathcal{E}}) = \tau^{-1} \begin{pmatrix} \overline{\mathbf{x}}_i - \widehat{\mathbf{x}}_i \\ \overline{t}_i - \widehat{t}_i \end{pmatrix}$$

In this case, the unconstrained problem is solved using L-BFGS [7].

## 5 Numerical Results

Next, we present numerical results for various methods discussed above, where we focus on four setups to test GEASI on theoretical and cardiac problems:

- 1 The square domain presented in Figure 1 with a periodic conduction velocity field, where the measurement domain  $\Gamma$  coincides with the boundary of the surface.
- 2 On a simplified 2D left ventricle (LV)-slice geometry with a transmural fiber rotation. Fiber and transverse velocities were set 0.6 and 0.4  $\frac{\text{m}}{\text{s}}$ , respectively. The measurement domain  $\Gamma$  is the outer ring of the domain, i.e. an epicardial slice.
- 3 On a clinically sampled, endocardial electrical mapping, measured during cardiac resynchronization therapy (CRT). The measurements were projected onto a patient-specific LV heart geometry and acquired by MRI. We mapped fiber orientations into the model using the approach described in [4]. Fiber, transverse and cross conduction velocities were set 0.6, 0.4 and 0.2  $\frac{\text{m}}{\text{s}}$ , respectively.
- 4 A full biventricular, trifascicular LV/RV human heart geometry with 1000 measurement points  $\Gamma$  distributed evenly along the epicardium. Fiber orientations were mapped as before. To account for the non-existent Purkinje fiber tree, an additional fast-conducting isotropic endocardial layer with a propagation velocity of 1.5  $\frac{\text{m}}{\text{s}}$  is used.

Further numerical specifications of the aforementioned setups are listed in Table 2. A summary of

	DOFs	Size [cm <sup>d</sup> ]	$h$ [mm]	Runtime [h]	Topological gradient	ECG
1	50 <sup>2</sup>	2 · 2	0.4	1/2 (ECG)	✓	✓
2	7980	2 · 2	0.11	1/2 (ECG)	✓	✓
3	1.5 · 10 <sup>4</sup>	10.7 · 8.9 · 9.5	1.9	2.5	✓	
4	1.08 · 10 <sup>5</sup>	10.3 · 8.1 · 12.6	0.66	3.5/18 (ECG)		✓

Table 2: Selected parameters for each setup. The size refers to the bounding box of the setups and  $h$  is the average element spacing. Tested extensions are indicated by check marks. The ECG runtimes are separately denoted behind the dash as the experiments are more computationally demanding.

the example setups is provided in Figure 7.

In this work, we use a custom C++ implementation of the FIM to solve (1). Note however that the method is independent of the chosen eikonal solver and may benefit from higher order or smoother solutions of different solvers. A minimal working example for the method can be found on GitHub<sup>1</sup>, but is limited to the isotropic eikonal equation on structured grids using the Fast Marching Method [37, 39] without FEM. The ECG and geodesic computations (see (22) and (11), respectively) and its Jacobian computation are calculated using the Tensorflow framework<sup>2</sup>, making use of available GPUs and enabling automatic derivation of  $V_i$  with respect to  $\widetilde{V}_m$ . All computations were performed on a single desktop machine with an Intel Core i7-5820K CPU using 6 cores of each 3.30GHz, 32GB of working memory and a NVidia RTX 2080 GPU.

## 5.1 Activation Time Optimization

In Figure 8, we present the results of GEASI for the 2D experiments: In the first iterations of the square example, the EASs are moved to the center of the domain to promote a good overall fit during optimization. As the sites approach the center, fine details on the boundary can be fitted by minimizing the mismatch defining the optimal points. The idealized LV model additionally requires a non-convex projection since the fiber alignment favors movements on the endocardial wall. The optimization still works for this case, even though the problem in (28) becomes non-convex.

Next, we concentrate on 3D experiments in Figures 9 and 10, for which we alter the number of initiation points for both models. Even though we can not ensure that the activation of the clinically acquired CRT patient can be described by the eikonal model with the simple rule-based

<sup>1</sup>[https://github.com/thomgrand/geasi\\_grid\\_demo](https://github.com/thomgrand/geasi_grid_demo)

<sup>2</sup><https://www.tensorflow.org/>

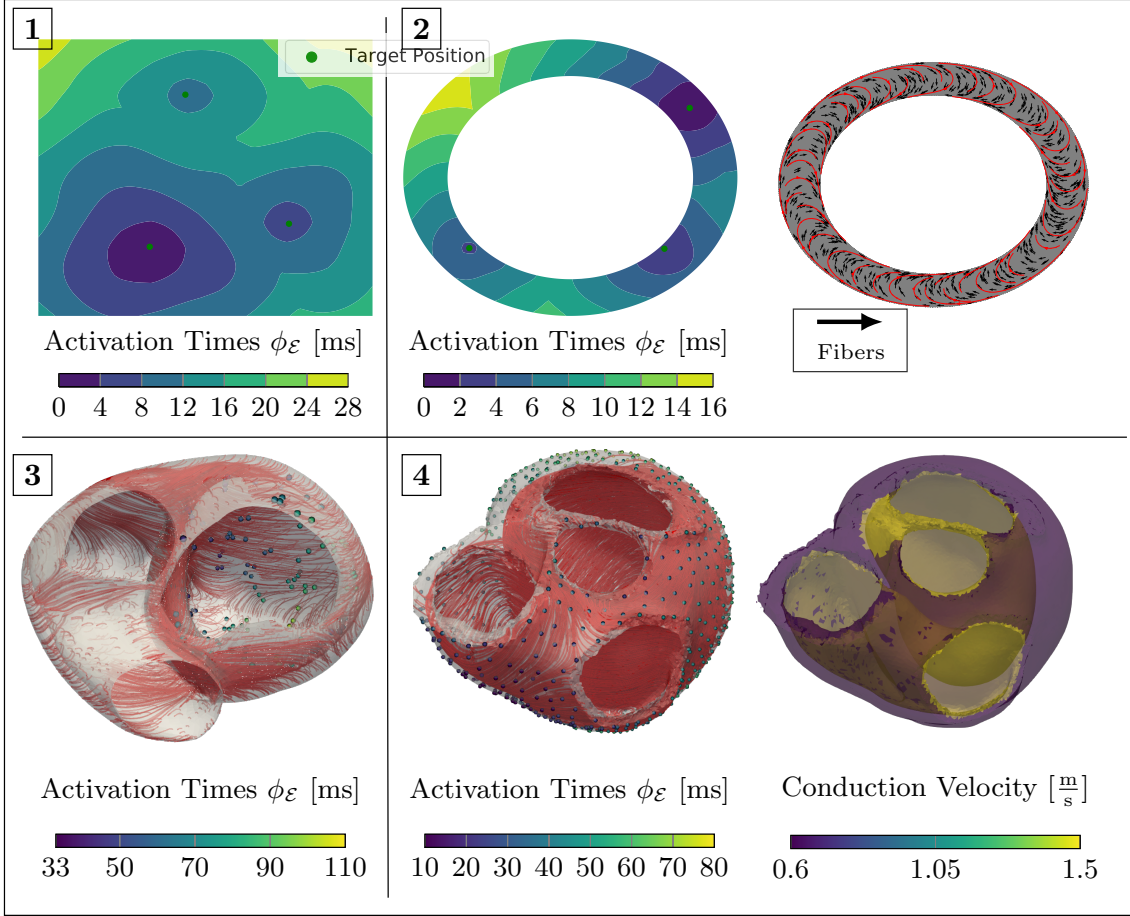


Figure 7: Activation times for all setups considered along with fiber orientations (if available). The isotropic conduction velocity of **1** is presented in Figure 1 and exhibits no fiber orientation due to isotropy. Note that **3** was measured in-vivo and thus no ground truth is available.

fiber orientation, the results on the CRT measurements provide an overall low root-mean-square error (RMSE) between modelled and measured activation times. In the presence of a single EAS, the fit is (expectedly) sub-optimal since the activation requires a more complex activation pattern. With three or more EASs, we get a much better fit, evenly distributed throughout the ventricles, but additional initiation sites are moved from the septum to the LV. These initiation sites seem to be an unrealistic consequence of the simplified modelling of fiber directions. We can achieve even better results by successively increasing the number of initiation sites, but this only reveals the nature of the ill-posed problem: By increasing the complexity of our model, we can more closely approximate the presented activation map (cf. Proposition 1).

The trifascicular model has a higher resolution in comparison to the CRT model with an added fast conducting sub-endocardial layer, which is utilized in all longer geodesics from the measurements to the initiation sites. For this reason, it is important to properly project the geodesics in each iteration on the endocardium in a fast way. For further details of the actual implementation we refer the reader to Section 6.2. As a result, when using less EASs than in the ground truth we already achieve convincing numerical results, which is visualized in Figure 10. If we incorporate 6 initiation sites, we get a very good fit, even though one of the activation sites is deactivated before convergence due to (6). The three septal points are jointly modelled by two EASs accounting for the deactivated point. Adding points beyond the given ones did not yield any improvement as they are deactivated by other points during the optimization (not shown).

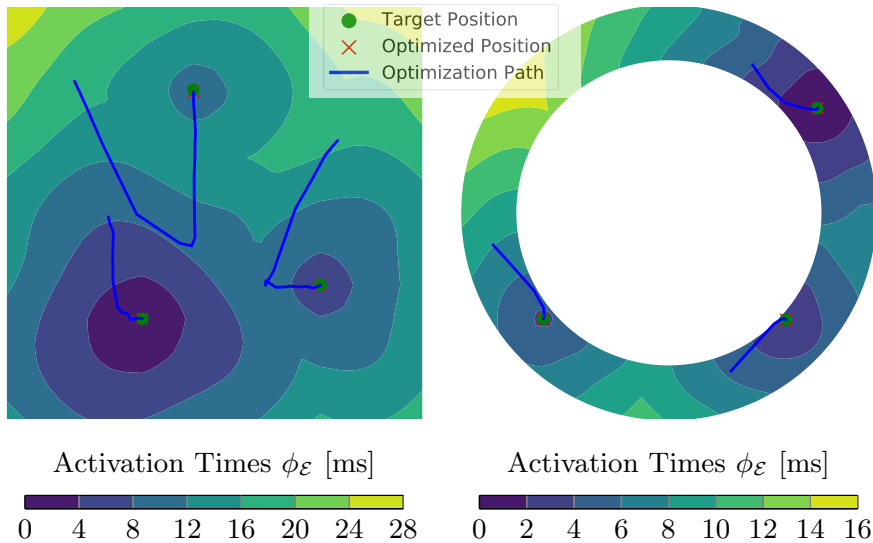


Figure 8: Results of GEASI for both 2D experiments. We located the exact initiation sites with only a few iterations, both for the heterogeneous velocity case (left) and in the presence of non-convex projections for the idealized LV model (right).

## 5.2 Topological Gradient

We also tried to estimate the correct number of EASs by using topological gradients (see Section 3.1), where we analyzed all 2D setups and the CRT patient. In this case, a splitting can only occur if the ratio  $\frac{\nu_{M,\epsilon}}{\nu_{S,\epsilon}}$  is below  $10^{-1}$  (2D)/ $2.5 \cdot 10^{-1}$  (3D) and the maximum Euclidean distance of the position of two consecutive iterates among all EASs is smaller than  $10^{-2}h$  (with  $h$  being the average element spacing).

The minimizer of (18) is chosen by evaluating 360 (2D)/5625 (3D) directions, which are evenly distributed on the hypersphere. We additionally ensure that the splitting direction is feasible (i.e. it does not point outside the domain) by projecting the samples onto the mesh. To avoid two coalescing EASs inside one element after a split, the points are moved apart by  $2h$  from the original site.

In Figure 11, we collected the results for all 2D experiments using this method and plot the ratio  $\frac{\nu_{M,\epsilon}}{\nu_{S,\epsilon}}$  over the iterations. The first EAS is moved towards the center of the ground truth EASs, and subsequently several splits occur that closely match the ground truth sites. A similar behavior can be observed in the idealized LV model.

For the CRT patient in Figure 12, neither the ground truth EASs nor the fiber distribution and velocities in  $\Omega$  are known. In total, the algorithm introduced 8 splits (i.e.  $N = 9$ ), of which 4 are deactivated during optimization since they violate (6). Only those final EASs are shown in the right plot of Figure 12. Moreover, we can see that three main clusters are identified, where one initiation cluster is located at the upper part of the anterior septum. The optimization in this region is further complicated by the very thin wall of the 3D mesh, which likely causes the high number of splits. We highlight that constant (in time) split ratios are caused by temporarily deactivated EASs violating (6). To conclude, we get a tremendous fit with the presented measurement points despite the aforementioned model assumptions. Moreover, the topological gradient could be successfully applied to all 2D models leading to the correct estimate for the number of EASs and also matching the correct sites. The corresponding results in 3D provide a very low overall RMSE on the measurements.

## 5.3 ECG

In what follows, we present numerical results for the ECG optimization for both 2D experiments as well as the trifascicular model in a simplified fashion as a proof-of-concept. The ECG requires



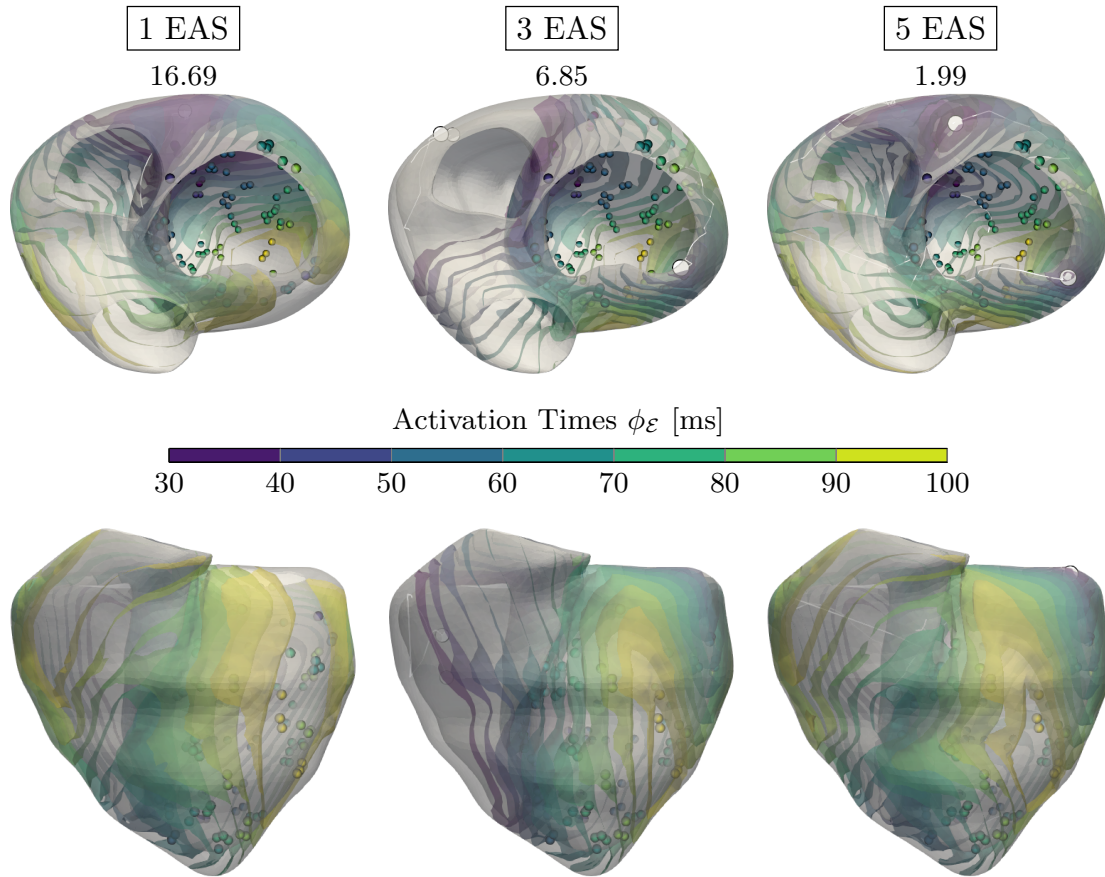


Figure 9: Results for the CRT experiment with varying number  $N$  of EASs along with the RMSE (in ms) shown above each experiment. The color-coded spheres indicate the observed activation times, while the white circles represent the optimized EAS positions. The white trailing paths show the optimization path over the iterations. Increasing  $N$  lowers the overall RMSE, but may result in physiologically unlikely EAS (e.g. top of the left ventricle for  $N = 5$ ).

an additional full torso domain  $\Omega_T$  and the computation of the lead fields. For all experiments in this paper, we submerge all three in-silico experiments (i.e. [1](#), [2](#), [3](#)) into a non-equilateral cube-torso without any additional organs and an overall torso conductivity of  $0.2 \frac{\text{S}}{\text{m}}$ . The size of the cube-torso is proportional to the bounding-box of  $\Omega$ . The computed lead fields are shown in Figure 13. In all cases, we generated a noiseless target ECG from the reference model setup with parameters and initiation sites already presented in Section 5. We optimize our model with random initialization with respect to this target ECG. Note that we do not focus on the generated ECGs' absolute potentials, since this heavily depends on the actual torso setup. Instead, we rather focus on the overall morphology of the ECGs.

To compute the lead fields in (23), our cube-torso is sampled using a structured regular grid of  $100^d$  equidistant points, and the problem is solved with a finite difference scheme. The lead fields are computed prior to the optimization since they remain constant. The ECG signals for the 3D models are mean-filtered with a small kernel of size  $\approx 2$  ms to improve accuracy.

Optimization solely based on the ECG is frequently very challenging. However, with a proper initialization  $(\mathbf{x}_i, t_i)$ , good fits for the ECGs can be computed. Figure 14 shows the optimization paths, as well as initial, target and optimized ECGs using the modified GEASI algorithm presented in Section 3.2 for the 2D examples, which are computed in approximately 2.5 hours each. The two potentials are a result of the two axis-aligned lead-fields (see Figure 13).

In the numerical experiments, it turned out that that the overall step size  $\beta_s$  has to be chosen smaller compared to the activation timing problem. The morphology of the initial ECG and the



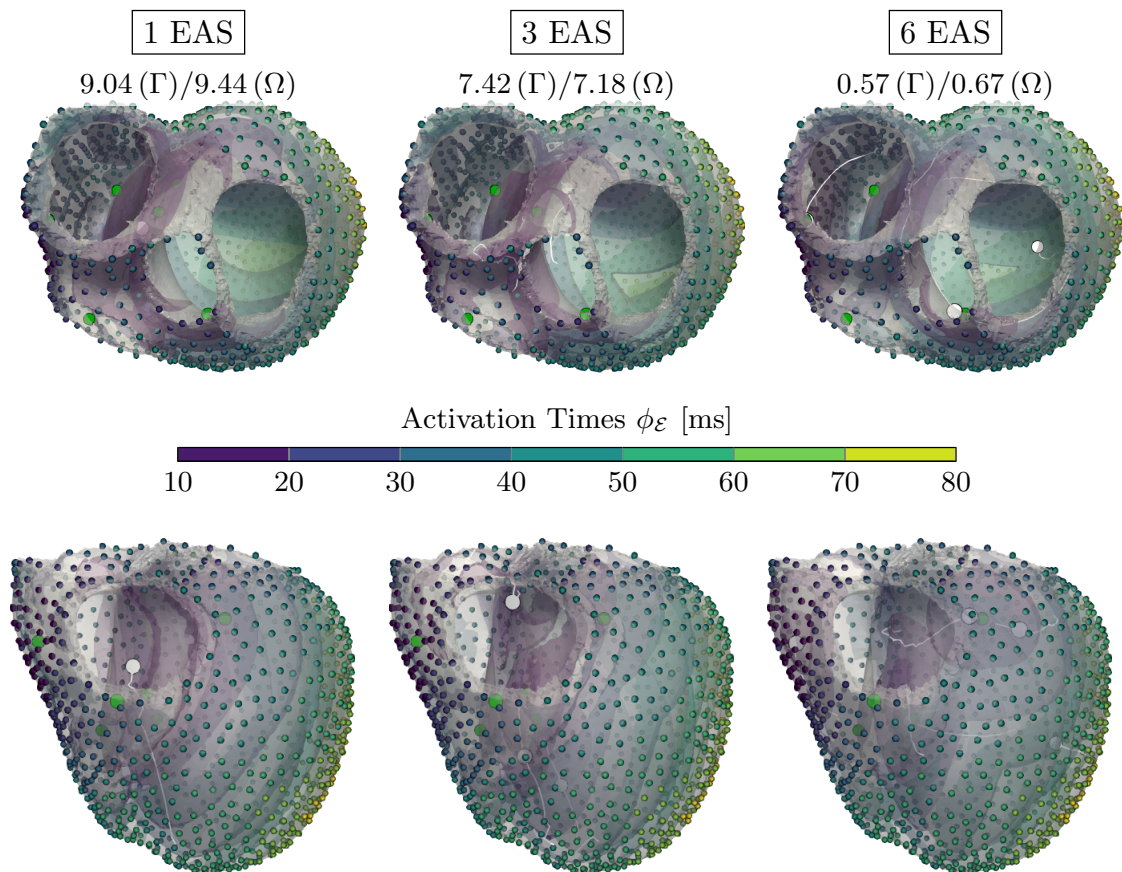


Figure 10: Results for the trifascicular experiment along with the RMSE (in ms) shown above the experiments for both  $\Gamma$  and  $\Omega$ . The color-coded spheres indicate the observed activation times. The white and green circles represent the optimized and target EAS, respectively. The overall RMSE activation error is very low if using the correct number of initiation sites ( $N = 6$ ), but we already obtain a good fit with fewer sites.

optimized ECG differ by a large margin, making the fitting non-trivial. As a result, in both the square domain and the idealized LV experiment we are able to closely match the actual sites from which the target ECG was generated (Figure 14, second row).

The trifascicular model in Figure 15 is computationally demanding since in each iteration step a computation of all geodesics is required, i.e. we need to solve  $\approx 10^5$  ODEs per iteration (for further details we refer to Section 6.2). As each initial EAS is randomly chosen, the initial ECG significantly differs from the target. Note that the 3D cube torso exhibits three axis-aligned leads. Since lead-X and lead-Z have the most prominent peaks, they have the largest effect on the resulting  $L^2$ -error. After the optimization, these peaks were fitted by the algorithm by shifting most of the initiation sites to the LV and one to the anterior wall and septal region. The added difficulty with an activation featuring that many EASs is also apparent from the computed paths (white lines) which strongly vary during optimization. After termination, 4 of 6 sites are close to the ground truth sites defining the target ECG.

## 6 Discussion

In the previous section, we have experimentally demonstrated the broad applicability of the proposed GEASI method for a variety of problems. Despite the convincing results there are still some issues related to our approach and alternative approaches, which will be addressed in future work.

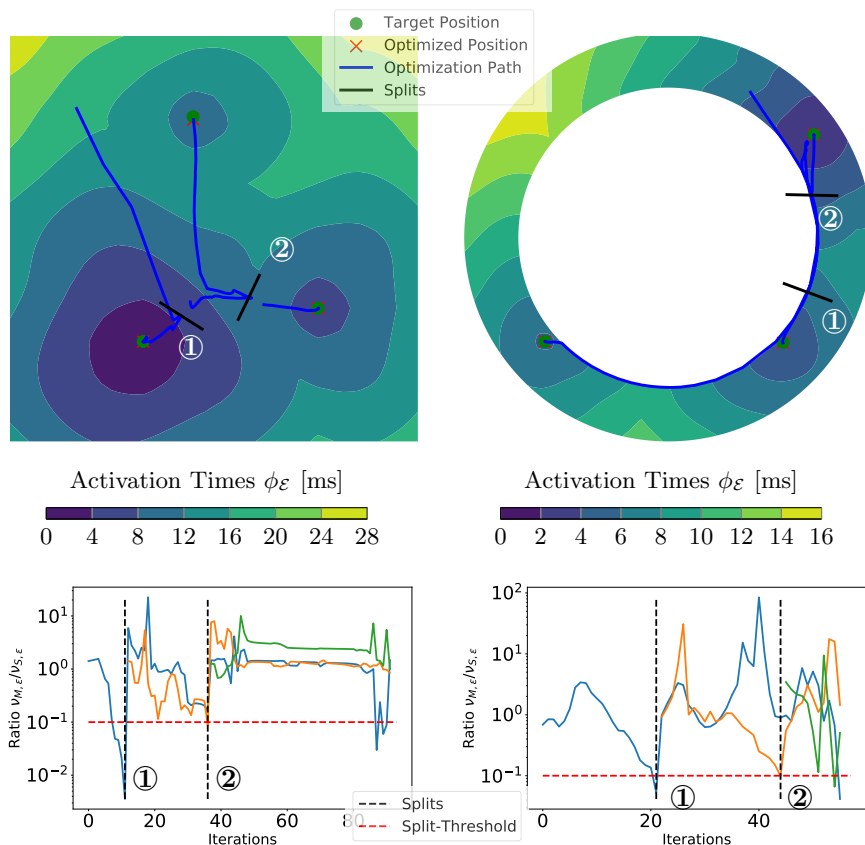


Figure 11: Results of the 2D experiments for the topological gradient. Top row: optimization paths starting with a single EAS. Bottom row: plots of  $\frac{v_{M,\epsilon}}{v_{S,\epsilon}}$  for each EAS depending on the iterations, where an EAS is split if this ratio is below the dotted red line. The location (top) and iteration (bottom) of the splits are marked by ① and ②. Note that an EAS only splits if all parameters have converged (see Section 5.2).

## 6.1 Eikonal Equation

In this work, we rely on the anisotropic eikonal equation, but other versions thereof are also applicable. More specifically, several eikonal frameworks to model physical and medical processes have been proposed over the last three decades, which can be derived from either the monodomain or the bidomain equation using a perturbation argument [12]. The most common equation inferred from a first-order approximation of the monodomain equation is the anisotropic eikonal equation (1). The eikonal model originating from the bidomain model is slightly different and is based on a Finsler-type metric [1].

Second-order approximations lead to the curvature-eikonal, diffusion-eikonal and viscous-eikonal equations. In the curvature-eikonal model [26], the front velocity is corrected by the curvature of the front in the metric induced by the conductivity tensor. In contrast, in the diffusion-eikonal equation [11] a diffusion term is added to the right-hand side of (1). Finally, in the viscous-eikonal model [27], a squared eikonal equation is considered, which is corrected by a diffusion term.

Higher-order approximations have also been proposed, but are rarely used in practice [16]. The effect of higher-order terms is more pronounced in front collisions, at the boundary of the domain and in narrow channels, e.g., in scarred tissue. In practice, however, deviations from the classical eikonal model are minimal and is therefore widely accepted for personalization of cardiac models.

The distinction between these models is however important from the point of view of the EASs and is often dictated by the numerical method rather than the physiology. In the standard anisotropic eikonal model (1), EASs can be single points, whereas in the curvature-eikonal equation EASs are required to have a strictly positive Lebesgue measure. Note that the conduction velocity

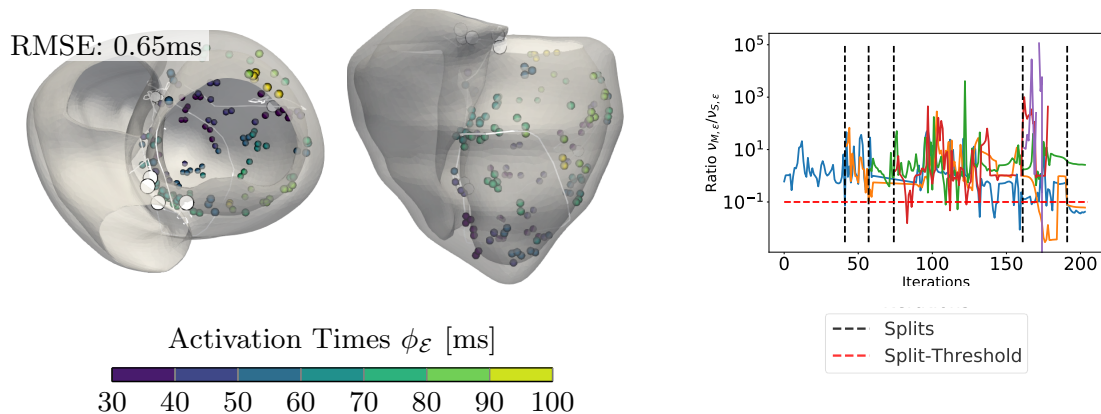


Figure 12: Results for the topological gradient extension on the CRT experiment with a visualization analogous to Figure 11.

of a spherical front with small radius is significantly slower in the presence of higher-order correction terms.

## 6.2 Runtime

The majority of the computational time is spent for solving the geodesics in (11), performed in parallel on the GPU. We highlight that the number of geodesics is proportional to the size of  $\Gamma$  in the original version (Algorithm 1) and proportional to  $\Omega$  in the modified version (Section 3.2). The computation of all geodesics in both cases is performed in parallel on a GPU and therefore scales well with the mesh size. The bulk of computational time inside the ODE solver is spent on the projection of each ODE solution back onto the mesh and nearest neighbor computation. For the nearest neighbor computation, we implemented a custom KD-Tree implementation (publicly available on GitHub<sup>3</sup>). For the projection operator, we extract the surface of the mesh, prior to the computation using the truncated signed distance function from VTK<sup>4</sup>. The K-nearest neighbor elements of the current positions of the geodesics are then queried to calculate the analytical projection onto all reference elements. The projection to all nearest neighbors is the minimum distance projection onto the mesh  $\Omega$ .

Solving the eikonal equation in (1) as well as the Gauss–Newton optimization in (13) only requires a minor portion of the computational time. As already mentioned, the activation time optimization is much faster compared to the remaining computations. In total, the experiments were finished within about 100 iterations only taking approximately 30 minutes and 90 minutes for 2D and 3D experiments, respectively. The experiments for the topological gradient behaves similarly regarding computational time. In contrast, the 3D optimization in the ECG problem requires approximately 12 hours.

To further decrease runtime, several approaches are possible: A custom GPU implementation to solve (11) along with the projection could significantly speed-up the optimization. Additionally, we often witnessed a collapse of many geodesic paths, especially in the trifascicular model, making subsequent computations redundant. An adaptive sampling from the measurement domain  $\Gamma$  combined with a proper upsampling technique could increase performance at the cost of precision.

To improve performance for the 3D ECG optimization, we analyzed the convergence of the ODEs. Figure 16 shows a probability density function (PDF) of convergence of the geodesics  $\gamma$  over the number of required iterations using the trifascicular model with a single initiation site in the septum. Convergence in this case is defined as the first time two subsequent ODE iterations of (11) have a change of less than  $10^{-10}$ , i.e.  $\|\gamma(t_{k+1}) - \gamma(t_k)\| < 10^{-10}$ . We see that many of the computed geodesics converge very quickly, while points with a high geodesic distance need

<sup>3</sup>[https://github.com/thomgrand/tf\\_kdtree](https://github.com/thomgrand/tf_kdtree)

<sup>4</sup><https://vtk.org/>

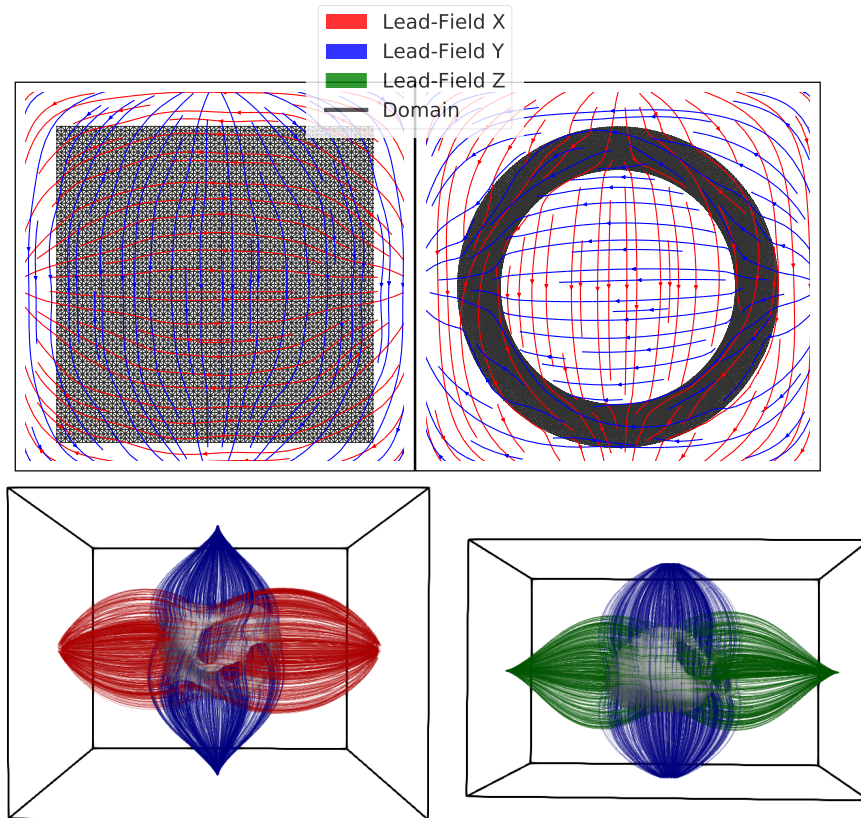


Figure 13: Setup for the ECG experiments showing the torso domain  $\Omega_T$ . The heart domain  $\Omega$  is indicated by black lines for the 2D experiments and gray silhouettes for 3D. The streamlines visualize the lead fields. Note that the lead field for axis Z (green) is only present in the 3D experiments.

significantly more iterations before convergence. Our vectorized/parallel implementation to solve (11) exploits this fact to only include non-converged geodesics.

### 6.3 ECG

The ECG results demonstrated that GEASI can be used to fit a given ECG. However, one main problem is getting stuck in local minima. While the  $L^2$ -error is relatively low in these minima, the morphology of the optimized and the target ECG differ a lot. One of the main reasons for this problem could result from the usage of the  $L^2$ -error, which is not robust to transformations of the time series, such as time shifts [43]. Better error measures for this type of optimization include dynamic time warping [36] and the Wasserstein distance [42, 8]. Finally, different optimization algorithms could further help to overcome this issue.

## 7 Conclusion and Future Work

This paper introduced the novel GEASI method to find the optimal source points of an eikonal model with a special focus on electrophysiological examples. We showed that GEASI can model complex eikonal activations, either from the activation times directly, or by fitting a given ECG. For our model examples, we were able to identify most of the ground truth EASs along with times, and in the case of the topological gradient also the number. We were even able to model CRT measured data with only a few source points.

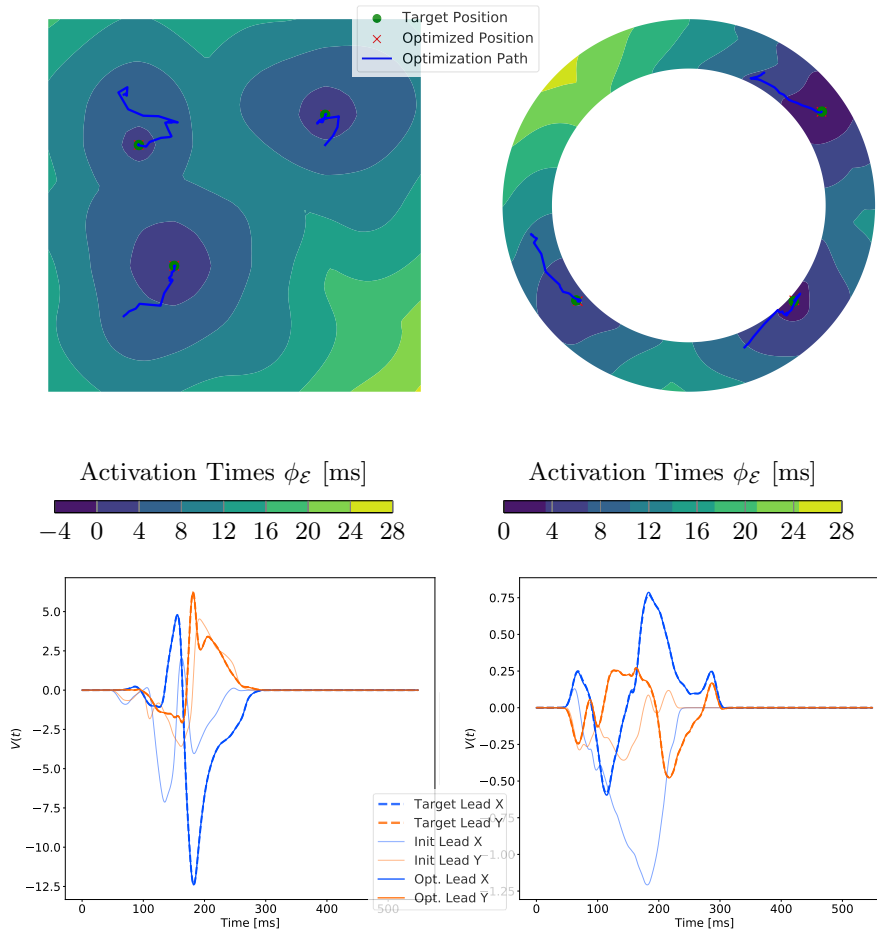


Figure 14: Results of the 2D ECG optimization. Top row: temporal change of the positions of the EASs along with the ground truth. Bottom row: initial, final and target ECG for fitting.

An alternative method for the computation of geodesics not incorporating the eikonal equation involves the method of characteristics [6, 18], which only necessitates solving the characteristic ODEs of the eikonal equation. This computationally challenging method heavily depends on the proper choice of the initial geodesic direction. As a benefit, this method is completely mesh-free, eliminating some of the potential issues discussed in Section 4.

So far, we only assumed fixed conduction velocities and fiber distributions for all cases. In future studies we intend to estimate these parameters using the same procedure with only minor necessary modifications to (13). We note that past studies [23, 24] have already shown that for the optimization of conductivities, additional regularization is crucial to decrease model complexity.

All extensions of GEASI such as topological gradient and ECG optimization hold much promise for future applications in clinical real-world examples. GEASI faces several computational hurdles, many of which we already tackled in this study. We hope to further improve and expand GEASI—both methodologically and computationally—to enlarge the applicability to a wide-range of problems. Therefore, we believe that GEASI has the potential to significantly advance and improve personalized health care in the future.

## Acknowledgements

This work was financially supported by the Theo Rossi di Montelera Foundation, the Metis Foundation Sergio Mantegazza, the Fidinam Foundation, the Horten Foundation and the CSCS—Swiss National Supercomputing Centre production grant s778. This research was supported by the grants



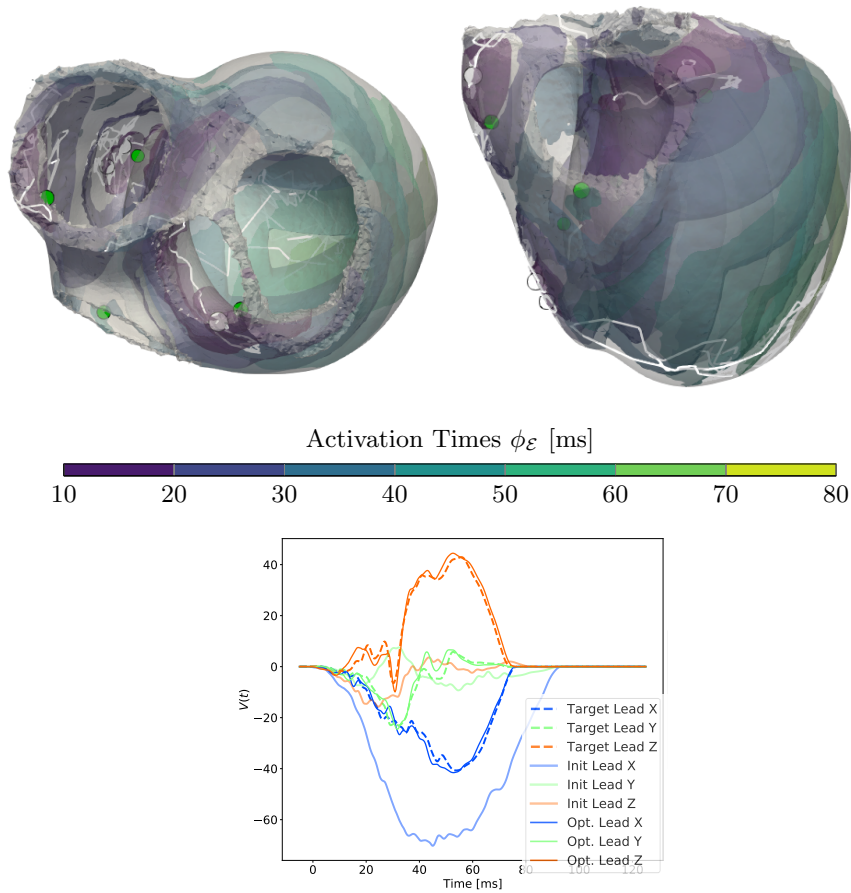


Figure 15: Results of the ECG optimization on the trifascicular model. Top row: optimized positions of EASs (white circles) along with temporal changes over the iterations (white lines). The green circles represent the target position from which the ground truth was generated. Bottom row: initial, final and target ECG.

F3210-N18 and I2760-B30 from the Austrian Science Fund (FWF) and BioTechMed Graz flagship award “ILearnHeart”, as well as ERC Starting grant HOMOVIS, No. 640156.

## References

- [1] L. Ambrosio, P. Colli Franzone, and G. Savaré. On the asymptotic behaviour of anisotropic energies arising in the cardiac bidomain model. *Interfaces Free Bound.*, 2(3):213–266, 2000.
- [2] F. Barber, I. García-Fernández, M. Lozano, and R. Sebastian. Automatic estimation of Purkinje-myocardial junction hot-spots from noisy endocardial samples: a simulation study. *Int. J. Numer. Methods Biomed. Eng.*, 34(7):e2988, 15, 2018.
- [3] A. Barone, A. Gizzi, F. Fenton, S. Filippi, and A. Veneziani. Experimental validation of a variational data assimilation procedure for estimating space-dependent cardiac conductivities. *Comput. Methods Appl. Mech. Engrg.*, 358:112615, 23, 2020.
- [4] J. D. Bayer, R. C. Blake, G. Plank, and N. A. Trayanova. A novel rule-based algorithm for assigning myocardial fiber orientation to computational heart models. *Annals of biomedical engineering*, 40:2243–2254, Oct. 2012.
- [5] F. Bornemann and C. Rasch. Finite-element discretization of static Hamilton-Jacobi equations based on a local variational principle. *Comput. Vis. Sci.*, 9(2):57–69, 2006.

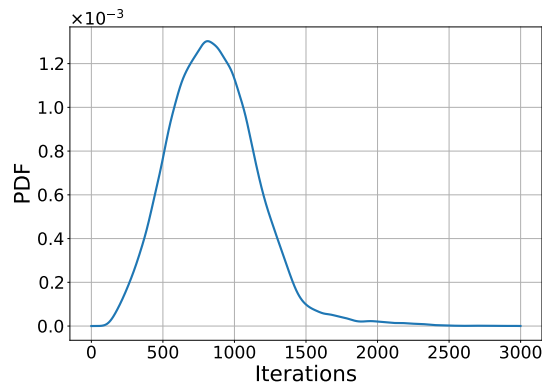


Figure 16: Convergence of the geodesic ODE in (11) for the trifascicular model over the iterations with a single EAS in the septum. The majority of the geodesics converge before 2000 iterations.

- [6] A. Bressan. Viscosity solutions of Hamilton–Jacobi equations and optimal control problems (lecture notes), 2003.
- [7] R. H. Byrd, P. Lu, J. Nocedal, and C. Y. Zhu. A limited memory algorithm for bound constrained optimization. *SIAM J. Sci. Comput.*, 16(5):1190–1208, 1995.
- [8] J. Camps, B. Lawson, C. Drovandi, A. Mincholé, Z. J. Wang, V. Grau, K. Burrage, and B. Rodriguez. Inference of ventricular activation properties from non-invasive electrocardiography. *arXiv:2010.15214*, Oct. 2020. arXiv: 2010.15214.
- [9] A. Chambolle and T. Pock. An introduction to continuous optimization for imaging. *Acta Numer.*, 25:161–319, 2016.
- [10] P. Colli Franzone and L. Guerri. Spreading of excitation in 3-d models of the anisotropic cardiac tissue. I. validation of the eikonal model. *Mathematical Biosciences*, 113(2):145–209, Feb. 1993.
- [11] P. Colli Franzone, L. Guerri, and S. Rovida. Wavefront propagation in an activation model of the anisotropic cardiac tissue: asymptotic analysis and numerical simulations. *J. Math. Biol.*, 28(2):121–176, 1990.
- [12] P. Colli Franzone, L. F. Pavarino, and S. Scacchi. *Mathematical cardiac electrophysiology*, volume 13 of *MS&A. Modeling, Simulation and Applications*. Springer, Cham, 2014.
- [13] J. Corral-Acero, F. Margara, M. Marciniak, C. Rodero, F. Loncaric, Y. Feng, A. Gilbert, J. F. Fernandes, H. A. Bukhari, A. Wajdan, M. V. Martinez, M. S. Santos, M. Shamohammdi, H. Luo, P. Westphal, P. Leeson, P. DiAchille, V. Gurev, M. Mayr, L. Geris, P. Pathmanathan, T. Morrison, R. Cornelussen, F. Prinzen, T. Delhaas, A. Doltra, M. Sitges, E. J. Vigmond, E. Zacur, V. Grau, B. Rodriguez, E. W. Remme, S. Niederer, P. Mortier, K. McLeod, M. Potse, E. Pueyo, A. Bueno-Orovio, and P. Lamata. The ‘Digital Twin’ to enable the vision of precision cardiology. *European Heart Journal*, 41(48):4556–4564, 03 2020.
- [14] F. S. Costabal, D. E. Hurtado, and E. Kuhl. Generating Purkinje networks in the human heart. *Journal of biomechanics*, 49(12):2455–2465, 2016.
- [15] M. G. Crandall, L. C. Evans, and P.-L. Lions. Some properties of viscosity solutions of Hamilton-Jacobi equations. *Trans. Amer. Math. Soc.*, 282(2):487–502, 1984.
- [16] H. Dierckx, O. Bernus, and H. Verschelde. Accurate eikonal-curvature relation for wave fronts in locally anisotropic reaction-diffusion systems. *Phys. Rev. Lett.*, 107(10):108101, 2011.
- [17] D. L. Donoho. De-noising by soft-thresholding. *IEEE Trans. Inform. Theory*, 41(3):613–627, 1995.

- [18] L. C. Evans. *Partial differential equations*, volume 19 of *Graduate Studies in Mathematics*. American Mathematical Society, Providence, RI, second edition, 2010.
- [19] Z. Fu, W.-K. Jeong, Y. Pan, R. M. Kirby, and R. T. Whitaker. A fast iterative method for solving the eikonal equation on triangulated surfaces. *SIAM J. Sci. Comput.*, 33(5):2468–2488, 2011.
- [20] Z. Fu, R. M. Kirby, and R. T. Whitaker. A fast iterative method for solving the eikonal equation on tetrahedral domains. *SIAM J. Sci. Comput.*, 35(5):C473–C494, 2013.
- [21] S. Giffard-Roisin, H. Delingette, T. Jackson, J. Webb, L. Fovargue, J. Lee, C. A. Rinaldi, R. Razavi, N. Ayache, and M. Sermesant. Transfer learning from simulations on a reference anatomy for ECGI in personalized cardiac resynchronization therapy. *IEEE Transactions on Biomedical Engineering*, 66(2):343–353, 2019.
- [22] D. Gilbarg and N. S. Trudinger. *Elliptic partial differential equations of second order*. Classics in Mathematics. Springer-Verlag, Berlin, 2001. Reprint of the 1998 edition.
- [23] T. Grandits, K. Gillette, A. Neic, J. Bayer, E. Vigmond, T. Pock, and G. Plank. An inverse Eikonal method for identifying ventricular activation sequences from epicardial activation maps. *J. Comput. Phys.*, 419:109700, 28, 2020.
- [24] T. Grandits, S. Pezzuto, J. M. Lubrecht, T. Pock, G. Plank, and R. Krause. PIEMAP: Personalized inverse eikonal model from cardiac electro-anatomical maps. In *Statistical Atlases and Computational Models of the Heart. M&Ms and EMIDEC Challenges*, pages 76–86, Cham, 2021. Springer International Publishing.
- [25] S. Kallhovd, M. M. Maleckar, and M. E. Rognes. Inverse estimation of cardiac activation times via gradient-based optimization. *International journal for numerical methods in biomedical engineering*, 34(2):e2919, 2018.
- [26] J. P. Keener. An eikonal-curvature equation for action potential propagation in myocardium. *J. Math. Biol.*, 29(7):629–651, 1991.
- [27] K. Kunisch, A. Neic, G. Plank, and P. Trautmann. Inverse localization of earliest cardiac activation sites from activation maps based on the viscous Eikonal equation. *J. Math. Biol.*, 79(6-7):2033–2068, 2019.
- [28] M. G. Larson and F. Bengzon. *The finite element method: theory, implementation, and applications*, volume 10 of *Texts in Computational Science and Engineering*. Springer, Heidelberg, 2013.
- [29] A. Lee, U. Nguyen, O. Razeghi, J. Gould, B. Sidhu, B. Sieniewicz, J. Behar, M. Mafi-Rad, G. Plank, F. Prinzen, C. Rinaldi, K. Vernooy, and S. Niederer. A rule-based method for predicting the electrical activation of the heart with cardiac resynchronization therapy from non-invasive clinical data. *Medical Image Analysis*, 57:197–213, 2019.
- [30] A. Neic, F. O. Campos, A. J. Prassl, S. A. Niederer, M. J. Bishop, E. J. Vigmond, and G. Plank. Efficient computation of electrograms and ECGs in human whole heart simulations using a reaction-eikonal model. *J. Comput. Phys.*, 346:191–211, 2017.
- [31] B. O’Neill. *Semi-Riemannian Geometry With Applications to Relativity, 103, Volume 103 (Pure and Applied Mathematics)*. Academic Press, 1983.
- [32] S. Palamara, C. Vergara, E. Faggiano, and F. Nobile. An effective algorithm for the generation of patient-specific Purkinje networks in computational electrocardiology. *J. Comput. Phys.*, 283:495–517, 2015.
- [33] S. Pezzuto, P. Kal’avský, M. Potse, F. W. Prinzen, A. Auricchio, and R. Krause. Evaluation of a Rapid Anisotropic Model for ECG Simulation. *Frontiers in Physiology*, 8:265, 2017.



- [34] S. Pezzuto, F. W. Prinzen, M. Potse, F. Maffessanti, F. Regoli, M. L. Caputo, G. Conte, R. Krause, and A. Auricchio. Reconstruction of three-dimensional biventricular activation based on the 12-lead electrocardiogram via patient-specific modelling, 2020. in press.
- [35] M. Potse, D. Krause, W. Kroon, R. Murzilli, S. Muzzarelli, F. Regoli, E. Caiani, F. W. Prinzen, R. Krause, and A. Auricchio. Patient-specific modelling of cardiac electrophysiology in heart-failure patients. *Europace : European pacing, arrhythmias, and cardiac electrophysiology : journal of the working groups on cardiac pacing, arrhythmias, and cardiac cellular electrophysiology of the European Society of Cardiology*, 16 Suppl 4:iv56–iv61, Nov. 2014.
- [36] H. Sakoe and S. Chiba. Dynamic programming algorithm optimization for spoken word recognition. *IEEE Transactions on Acoustics, Speech, and Signal Processing*, 26(1):43–49, Feb. 1978. Conference Name: IEEE Transactions on Acoustics, Speech, and Signal Processing.
- [37] J. A. Sethian. A fast marching level set method for monotonically advancing fronts. *Proc. Nat. Acad. Sci. U.S.A.*, 93(4):1591–1595, 1996.
- [38] S. Stella, C. Vergara, M. Maines, D. Catanzariti, P. C. Africa, C. Demattè, M. Centonze, F. Nobile, M. Del Greco, and A. Quarteroni. Integration of activation maps of epicardial veins in computational cardiac electrophysiology. *Computers in Biology and Medicine*, page 104047, 2020.
- [39] J. N. Tsitsiklis. Efficient algorithms for globally optimal trajectories. *IEEE Trans. Automat. Control*, 40(9):1528–1538, 1995.
- [40] J. N. Ulysses, L. A. Berg, E. M. Cherry, B. R. Liu, R. W. d. Santos, B. G. d. Barros, B. M. Rocha, and R. A. B. d. Queiroz. An Optimization-Based Algorithm for the Construction of Cardiac Purkinje Network Models. *IEEE Transactions on Biomedical Engineering*, 65(12):2760–2768, Dec. 2018.
- [41] E. J. Vigmond and B. D. Stuyvers. Modeling our understanding of the his-purkinje system. *Progress in biophysics and molecular biology*, 120(1-3):179–188, 2016.
- [42] C. Villani. *Optimal transport*, volume 338 of *Grundlehren der Mathematischen Wissenschaften [Fundamental Principles of Mathematical Sciences]*. Springer-Verlag, Berlin, 2009. Old and new.
- [43] Y. Yang, B. Engquist, J. Sun, and B. F. Hamfeldt. Application of optimal transport and the quadratic Wasserstein metric to full-waveform inversion. *GEOPHYSICS*, 83(1):R43–R62, Oct. 2017. Publisher: Society of Exploration Geophysicists.